

RELAXATION MAPPING IN MAGNETIC PARTICLE IMAGING

A THESIS SUBMITTED TO
THE GRADUATE SCHOOL OF ENGINEERING AND SCIENCE
OF BILKENT UNIVERSITY
IN PARTIAL FULFILLMENT OF THE REQUIREMENTS FOR
THE DEGREE OF
MASTER OF SCIENCE
IN
ELECTRICAL AND ELECTRONICS ENGINEERING

By
Yavuz Muslu
January 2018

RELAXATION MAPPING IN
MAGNETIC PARTICLE IMAGING

By Yavuz Muslu

January 2018

We certify that we have read this thesis and that in our opinion it is fully adequate,
in scope and in quality, as a thesis for the degree of Master of Science.

Emine Ülkü Sarıtaş Çukur (Advisor)

Ergin Atalar

Nevzat Güneri Gençer

Approved for the Graduate School of Engineering and Science:

Ezhan Kardeşan
Director of the Graduate School

ABSTRACT

RELAXATION MAPPING IN MAGNETIC PARTICLE IMAGING

Yavuz Muslu

M.S. in Electrical and Electronics Engineering

Advisor: Emine Ülkü Sarıtaş Çukur

January 2018

Magnetic Particle Imaging (MPI) is a novel biomedical imaging modality that shows great potential in terms of sensitivity, resolution, and contrast. Since its first introduction in 2005, several applications of MPI have already been demonstrated such as angiography, stem cell tracking, and cancer imaging. Recently, multi-color MPI techniques have been proposed to increase the functionality of MPI, where different nanoparticles are distinguished according to the differences in their responses to oscillating magnetic fields. These methods can also be extended to probe environmental factors such as viscosity and temperature, provided that the responses of different nanoparticles or nanoparticles in different environments are pre-calibrated. This thesis proposes a new multi-color MPI technique that does not require a calibration phase. This new technique directly estimates the relaxation time constants of nanoparticles to distinguish nanoparticle types and environmental factors from the MPI signal, and generates a multi-color relaxation map. The validity of the proposed technique is confirmed through an extensive experimental work with an in-house Magnetic Particle Spectrometer (MPS) at 10.8 kHz and an in-house MPI scanner at 9.7 kHz drive field frequencies, successfully distinguishing different nanoparticle types. The proposed calibration-free multi-color MPI technique is a promising method for future functional imaging applications of MPI.

Keywords: Magnetic Particle Imaging, Multi-Color MPI, Magnetic Nanoparticle Relaxation, Direct Estimation, Mirror Symmetry.

ÖZET

MANYETİK PARÇACIK GÖRÜNTÜLEMEDE RELAKSASYON HARİTALAMA

Yavuz Muslu

Elektrik Elektronik Mühendisliği, Yüksek Lisans

Tez Danışmanı: Emine Ülkü Sarıtaş Çukur

Ocak 2018

Manyetik Parçacık Görüntüleme (MPG) duyarlılık, çözünürlük ve kontrast açısından yüksek potansiyel gösteren yeni bir biyomedikal görüntüleme yöntemidir. 2005'teki ilk sunuluşundan bu yana, MPG'nin anjiyografi, kök hücre takibi ve kanser görüntüleme gibi birçok uygulaması deneysel olarak gösterilmiştir. Yakın zamanda renkli MPG teknikleri önerilmiş ve manyetik alan değişimlerine farklı tepkiler veren nanoparçacıkların ayırt edilmesi sağlanmıştır. Bu teknikler sıcaklık ve viskozite gibi ortam özelliklerini ayırt edecek şekilde genişletilebilmektedir, ama bunun için farklı nanoparçacık tepkilerinin kalibrasyonunun önceden yapılması gerekmektedir. Bu tezde kalibrasyon gerektirmeyen yeni bir renkli MPG tekniği önerilmektedir. Bu teknik, nanoparçacıkların relaksasyon zaman sabitini doğrudan MPG sinyalinden hesaplayıp, farklı nanoparçacıkları ve ortam özelliklerini ayırt etmektedir. Önerilen teknik, özel olarak tasarlanmış bir manyetik parçacık spektrometre (MPS) düzeneği ile 10.8 kHz frekansta ve özel olarak tasarlanmış bir MPG tarayıcısında 9.7 kHz frekansta deneyler ile gösterilmiştir. Bu deneylerde 3 farklı nanoparçacık tipinin başarıyla ayırt edilmesi sağlanmıştır. Önerilen kalibrasyonsuz renkli MPG tekniği, MPG'nin gelecekteki fonksiyonel görüntüleme uygulamaları için umut veren bir yöntemdir.

Anahtar sözcükler: Manyetik Parçacık Görüntüleme, Renkli MPG, Manyetik Nanoparçacık Relaksasyonu.

Acknowledgement

Completing my undergraduate education brought up more questions than it answered, in terms of the career path that I wanted to choose. Although I had certain academic interests and subjects that I found closer to me, it was not until the graduate admissions that I realized my passion for biomedical engineering. For that, I feel very fortunate to have met my master's degree advisor, Emine Ülkü Sarıtaş, before the graduate school admissions. During the admission interviews and she took the time to explain her research field and answered my questions patiently. Because of her understanding and thoughtful attitude during the interviews, I felt very comfortable taking the graduate student position under her supervision. She cares about her students immensely, spares no effort to guide them through their research, and shares her knowledge and experience very generously. She welcomes questions anytime her students need help but motivates them to become independent researchers. She is the most thoughtful, selfless and kindest advisor anyone can hope for, and it was a privilege to have worked with her during my graduate studies.

I would like to thank Ergin Atalar and Nevzat Güneri Gençer for taking the time to be in my master's degree thesis committee. Their feedbacks and discussions were very valuable, and will surely affect the future of this study positively.

I would like to thank the following funding agencies for supporting the work in this thesis: the Scientific and Technological Research Council of Turkey through TUBITAK Grants 114E167 and 115E677, the European Commission through FP7 Marie Curie Career Integration Grant (PCIG13-GA-2013-618834), the Turkish Academy of Sciences through TUBA-GEBIP 2015 program, and the BAGEP Award of the Science Academy.

I would also like to thank my research group mates, who are also close friends: Alper Özaslan, Çağla Deniz Bahadır, Damla Sarıca, Ecem Bozkurt, Mustafa Ütkür, Ömer Burak Demirel, Sevgi Gökçe Kafalı, and Toygan Kılıç. They were always kind, helpful and a lot of fun. Mustafa and Burak spent lots of time

with me in the lab trying to figure out what was wrong with the experiment setup, which, in the end, provided some of the funniest and most fulfilling memories of my graduate life. Although we could not realize Burak’s minimalist design plans for our setup, which included significant amount of woodwork, it was really fun to work with them. Whenever I needed a break from the research, Toygan and Alper were always there for me to either distract with my nonsense or start some serious discussions about their research. Çağla kept my ties with art and literature alive with her brilliant suggestions on classical music, plays and books. Going to the theater with her always gave me a peace of mind even when there were a lot of work to be completed in the lab.

I would also like to thank my cubicle mates, or as we would call ourselves “the champion cubicle”: Akbar Alipour, Koray Ertan, Cemre Arıyürek, Mustafa Ütkür, and Sevgi Gökçe Kafalı. Their sense of humor picked me up whenever I felt tired or frustrated. Koray provided some interesting and enjoyable discussions with his funny but spot on takes on life. Sevgi, having gone through similar stages in our graduate studies, was always very understanding and helpful. It was also very motivating to set ourselves some serious challenges on the completion of our research projects, which *definitely* helped all of us. Akbar Alipour never failed to make us feel guilty with his organized and extremely healthy life style. Efe and Özgür made our office a more fun place to be around, which helped a lot when I needed to work in the evenings or weekends.

I would like to thank Seçkin and Barış for helping me throughout my graduate studies. Whenever I wanted to improve my knowledge on politics or economics, or clear my head with some funny anecdotes, I could count on them to be there for me. I enjoyed our discussions on the investments that we never had and the money that we never made via those investments. Although our ideas conflicted at times, we have learned a lot from each other.

Finally, I would like to thank my family for their endless support throughout my graduate studies. They were always by my side whenever I needed help. It is because of their support and trust in me, that I found the motivation to keep moving forward in difficult times. I would like to thank, especially my brother

Kerem. Due to the similar career paths we select, I could always share the difficulties that I face and expect a sound suggestion from him. After providing one, he would never miss the opportunity to make fun of me a little bit just to remind me to take the life easier. I would not be able to complete my thesis without their help and support, that is why I will always be grateful to them.

Yavuz Muslu

January 2018

Contents

1	Introduction	1
2	Background and Theory	4
2.1	Magnetic Particle Imaging Physics	4
2.1.1	Spatial Encoding	4
2.1.2	1D MPI Signal Equation	5
2.1.3	SPIO Relaxation	8
2.2	Image Reconstruction Methods	9
2.2.1	System Function Reconstruction	9
2.2.2	X-space Reconstruction	10
2.3	Multi-color Magnetic Particle Imaging	12
3	Direct Relaxation Time Constant Estimation	14
3.1	Theory	14

3.2	Simultaneous Hardware Delay and Relaxation Time Constant Estimation	18
3.3	Magnetic Particle Spectrometer Experiments	19
3.3.1	MPS Setup	19
3.3.2	Sample Preparation	21
3.4	Results	21
4	Calibration-Free Multi-Color MPI	24
4.1	Algorithm	24
4.2	1D and 2D Simulations	28
4.2.1	Methods	28
4.2.2	Results	29
4.3	Magnetic Particle Imaging Experiments	32
4.3.1	MPI Scanner	32
4.3.2	Sample Preparation	34
4.3.3	Results	35
5	Discussion	39
5.1	Effects of SPIO Types and Imaging Parameters	40
5.2	Resolution of the Relaxation Map	40
5.3	Fine Tuning of the Hardware Delays	41

<i>CONTENTS</i>	x
5.4 Towards True Quantitative MPI	42
5.5 Extensions to 2D/3D Excitation and FFL Scanners	42
6 Conclusion	44
A Relaxation Time Constant of a Homogeneous Mixture	52
B Effects of pFOV overlap on the Relaxation Map	54
C Local Minima Analysis	56
C.1 The Effects of Hardware Delays	56
C.2 Uniqueness of Local Minimum	58
D Noise Analysis	59

List of Figures

- 2.1 Nonlinear magnetization curve of SPIOs. Horizontal axis (H) shows the external magnetic field, vertical axis (M) shows the SPIO magnetization. M_{sat} denotes the saturation magnetization of SPIOs. 5
- 2.2 (a) Topology of an MPI scanner, where black circles denote selection field coils. Here, blue arrows denote the magnetic field lines and their directions. Orange dot denotes the FFP, while yellow dot denotes a region where the SPIOs are saturated by the selection field. (b) Comparison of signals acquired from SPIOs that are unsaturated (orange) and saturated (yellow) by the selection field. Here, orange and yellow regions experience the same sinusoidal drive field, with a different selection field component. When particles are not saturated, they induce a signal on the receive coil (orange plots). When the particles are saturated, they cannot react to the sinusoidal drive field and cannot induce a signal on the receive coil (yellow plots). 6

2.3 (a) Illustration of Brownian and Neel relaxations. Initially magnetic moments of the SPIOs are aligned with the horizontal external magnetic field. When external magnetic field is rotated, SPIOs physically rotate to align their magnetization via the Brownian relaxation process, and/or SPIOs change the direction of their magnetic moments internally via the Neel relaxation process. (b) MPI signal with and without relaxation. Here adiabatic signal denotes the MPI signal without relaxation, and nonadiabatic signal denotes the MPI signal with relaxation. Due to the relaxation effects, the MPI signal lags (peak of the signal shifts in time), widens, and loses SNR (peak amplitude of the signal decreases). 8

2.4 Illustration of calibration measurement for SFR. Here, calibration for one pixel location is illustrated. Red dot denotes a point source that is used for calibration. Blue curve denotes the FFP trajectory that scans the entire FOV. Once the signal is acquired with this FFP trajectory, Fourier transform of this measurement is recorded to the a column of the system matrix. Each column in the system matrix corresponds to a calibration measurement from one pixel. Overall calibration procedure includes the calibration measurements for every pixel in the FOV. 10

2.5 Illustration of X-space Reconstruction. (a) An example circular SPIO distribution. (b) Multidimensional PSF of the MPI system. (c) Image obtained with the x-space reconstruction. The resulting image shows the SPIO distribution blurred by the PSF of the system. 11

3.1 The mirror symmetry of the adiabatic MPI signal and how the relaxation effects break that mirror symmetry. (a) A ramp-shaped nanoparticle density. (b) The corresponding ideal MPI image obtained by the convolution of nanoparticle density and the point spread function. (c) Adiabatic vs. non-adiabatic MPI signals for a ramp-shaped nanoparticle density. Here, one full periods of the signals are shown (i.e., the signals from both the negative and positive cycles). (d) In the adiabatic case, due to the repetitive nature of applied sinusoidal drive field, positive and mirrored negative signals match perfectly. This phenomenon is referred as "mirror symmetry". (e) The relaxation effect causes an asymmetric blurring of the negative and positive signals, which in turn breaks the mirror symmetry. 16

3.2 The proposed method: direct relaxation time constant estimation. (a) The mirror symmetry between the positive and negative signals is broken due to relaxation. The proposed method estimated $\hat{\tau} = 6.96 \mu s$, where $\tau = 7 \mu s$ in theory. (b) MPI signal is then deconvolved with the estimated relaxation kernel using $\hat{\tau} = 6.96 \mu s$, which recovers the underlying mirror symmetry. Here, (a, b) demonstrate the case where the fundamental frequency is kept intact in simulations, and (c, d) demonstrate the case after direct feedthrough filtering that removes the fundamental frequency. In the latter case, the estimation resulted in $\hat{\tau} = 6.99 \mu s$ 17

3.3 Experimental relaxation time constant estimation algorithm. (a) A time point t_{edge} is chosen to mark the time when positive scan finishes and negative scan starts. Then, τ is estimated for different t_{edge} values chosen from $[0, T/2)$ interval. The MSE between the deconvolved positive and mirrored negative signals are computed for each case. (b) The MSE values are compared, and the (τ, t_{edge}) pair that minimizes MSE is chosen as the solution. For this example, the result is $\hat{\tau} = 3.51 \mu s$. Here, the black arrows show the flow of the algorithm, while blue arrows show a visual demonstration of each step. 20

3.4 Experimental demonstration in the MPS setup. (a) Picture of our in-house MPS setup, showing the drive and receive coils placed co-axially. (b) Signal acquired from Nanomag-MIP (blue) and VivoTrax (orange) SPIOs, and their homogeneous mixture (yellow). The Nanomag-MIP and VivoTrax SPIOs yielded $\hat{\tau} = 3.28 \mu s$ and $\hat{\tau} = 4.46 \mu s$, respectively. 22

3.5 Experimental demonstration of the homogeneous mixture case in the MPS setup. (a) Picture of our in-house MPS setup, showing the drive and receive coils placed co-axially. (b) Signal acquired from Nanomag-MIP (blue) and VivoTrax (orange) SPIOs, and their homogeneous mixture (yellow). The Nanomag-MIP and VivoTrax SPIOs yielded $\hat{\tau} = 3.28 \mu s$ and $\hat{\tau} = 4.46 \mu s$, respectively. The homogeneous mixture gave $\hat{\tau} = 3.89 \mu s$, closely matching the expected value of $3.87 \mu s$ based on the average of the Nanomag-MIP and VivoTrax relaxation times. 23

4.1 The proposed relaxation mapping algorithm. (a) The simulated particle distributions for two different SPIO types, which overlap in a small region in 1D space. (b) The x-space reconstructed MPI image. (c) Signal RMS values for each pFOV. (d) The initial relaxation time constant estimations are plotted as a histogram, and (e) the histogram is corrected by eliminating low SNR regions and overestimations (i.e., an upper threshold set at $T/4$). (f) A k-means clustering detects two main clusters (shown in orange and red). (g) These regions are highlighted in the initial τ map. (h) The inhomogeneous nanoparticle mixture region is detected, and (i) the final τ map is achieved via modeling the transition using a smooth sigmoid curve and setting low pixel intensity regions to zero. Note the change in y-axis scaling from (h) to (i). 26

4.2 Results of 1D simulations for three different cases for SNR=5, without signal averaging. Left column (a, d, g) demonstrates the spatial distributions for different SPIOs with relaxation time constants ranging between 1-5 μs . Middle column (b, e, h) demonstrates the corresponding x-space MPI images. Right column (c, f, i) demonstrates the relaxation maps reconstructed with the proposed algorithm. The mean estimation error is well below 3% for (c), and is around 7% for (i) due to reduced distances between the different SPIO distributions. 30

4.3 Results of 3D simulations, for SNR=5. (a) A distribution with homogeneous mixtures of 2.9 μs and 1.1 μs SPIOs in different concentrations. Each mixture is labeled with a number from 1 to 9, with concentrations of 2.9 μs SPIO in each mixture given as (100, 87.5, 75, 62.5, 50, 37.5, 25, 12.5, 0)%, respectively. (b) The x-space MPI image, and (c) the color overlay of the multi-color relaxation map and the MPI image. (d) The estimated time constants vs. relative concentrations of the two SPIOs. Here, the error bars denote the standard deviations for each ROI, and the red dashed curve is the fitted line (with $R^2 = 0.9921$). FOV size is $9 \times 9 \text{ cm}^2$. The Euclidean distance between neighboring samples is 1.7 cm. 31

4.4 An overview of the MPI scanner and the experimental setup. (a) The entire imaging system is controlled through MATLAB, via a custom MPI imaging toolbox. First, robot position is adjusted to place the phantom at the desired location. Second, a drive field at 9.7 kHz is applied through the transmit chain, and the nanoparticle signal is simultaneously acquired through the receive chain. (b-c) Front and side views of our in-house MPI scanner. The phantoms imaged in (d) the 1D experiment and (e) the 2D experiment. . . . 33

4.5 Calibration-free multi-color MPI results in 1D. The imaging experiment was conducted at 9.7 kHz and 15 mT-peak drive field, using three different nanoparticles. (a) 1D reconstructed x-space MPI image, and (b) the corresponding multi-color relaxation map. (c) The color overlay of the MPI image and the multi-color map shows that the nanoparticles can be clearly distinguished based on their relaxation responses. (d) A photo of the imaged phantom with three tubes containing Perimag, VivoTrax and Nanomag-MIP SPIOs from left to right, separated at 8mm distances. 36

- 4.6 Calibration-free multi-color MPI results in 2D. The imaging experiment was conducted at 9.7 kHz and 15 mT-peak drive field, using Nanomag-MIP and VivoTrax SPIOs, and their homogeneous mixture. (a) The reconstructed x-space MPI image and (b) the corresponding multi-color relaxation map. (c) The color overlay of the MPI image and the multi-color map shows that the two nanoparticles and their homogeneous mixture can be clearly distinguished in 2D, solely based on their relaxation responses. The mixture yields a τ value that closely matches the signal-weighted average of the τ values from Nanomag-MIP and VivoTrax. (d) A photo of the imaged phantom with three tubes containing VivoTrax, the homogeneous mixture, and Nanomag-MIP from left to right, separated at 15 mm distances. 38
- B.1 Results of the resolution study. (a) Nanoparticle distributions with two distinct τ values. Each row demonstrates a simulation result for a different pFOV overlap (e.g. 90%, 80%, 60% and 40%). For the first two rows, the resolution of the MPI system is larger than the spatial overlap (or pixel size) of the pFOVs. As such, the resolution of the relaxation map is equal to the resolution of the MPI system. For the last two rows, the pixel size of the relaxation map is larger than the resolution of the MPI system. Accordingly, the resolution of the relaxation map is equal to the pixel size of the relaxation map. 55
- C.1 Simulation results for the uniqueness of the local minimum of Eq. 3.9. Here, the logarithm of the MSE between the positive and mirrored negative signals after the deconvolution is calculated across different (τ, t_{edge}) pairs. The vertical axes show the range of t_{edge} , while the horizontal axes show the range of τ values. The simulation results for the actual pairs of (a) $(\tau, t_{\text{edge}})_{\text{actual}} = (1 \mu\text{s}, 0)$, (b) $(\tau, t_{\text{edge}})_{\text{actual}} = (3 \mu\text{s}, 0)$, and (c) $(\tau, t_{\text{edge}})_{\text{actual}} = (5 \mu\text{s}, 0)$. The correct pairs that minimize Eq. 3.9 are shown with red arrows. 58

- D.1 Simulation results for the robustness of the proposed relaxation time constant estimation technique against noise. Here standard deviations of the estimated τ values are calculated across different SNR values. The vertical axes show the range of estimated τ , while the horizontal axes show the range of SNR values. Standard deviations for the actual time constant of (a) $\tau_{actual} = 1 \mu s$, (b) $\tau_{actual} = 3 \mu s$, and (c) $\tau_{actual} = 5 \mu s$ 60
- D.2 Simulation results for the robustness of the proposed calibration-free multi-color MPI algorithm against noise. Each row demonstrates a simulation result for a different SNR value (e.g. 50, 10, 5, and 2). (a) Nanoparticle distributions with two distinct τ values. (c, e) For larger SNR values (e.g., SNR=10), results of the proposed mapping algorithm do not show significant deviations from each other. (g) For SNR=5 case, relaxation map shows very small, noise-like distortions, however shape of the map is still similar to that of SNR=50 case. (i) For SNR=2 case, there are larger deviations from the ideal map, but the results are still fairly accurate. 61

Chapter 1

Introduction

Magnetic Particle Imaging (MPI) is a novel and rapidly developing imaging modality that shows great potential in terms of resolution, contrast, and sensitivity [1, 2, 3, 4, 5]. Since its first introduction in 2005, several applications of MPI have already been demonstrated such as angiography [6, 7], stem-cell tracking [8, 9, 10], cardiovascular interventions [11], and cancer imaging [12]. MPI detects and images the spatial distribution of super paramagnetic iron oxide (SPIO) nanoparticles in a field-of-view (FOV) by utilizing a combination of three different magnetic fields. First, a temporally constant selection field with a strong gradient is used to provide a spatial encoding inside the imaging volume. This selection field is obtained by placing two very strong magnets such that the north poles of the magnets face each other. This configuration creates a zero-field region at the center of the scanner setup, this region is called the field-free point (FFP) or the field-free line (FFL) depending on the topology of the magnets. Next, an oscillating drive field is applied to move the FFP rapidly, changing the magnetization of SPIOs in a small region inside the FOV. This change in the SPIO magnetization induces a signal, which is then collected via a receive coil. Due to human safety limits, drive field alone is not enough to cover the entire FOV, necessitating a partitioning of the FOV called partial field-of-views (pFOVs) [13, 14, 15, 16, 17]. Hence, low-frequency but higher amplitude focus fields are used to shift the FFP to regions that cannot be covered with the drive

field alone [18, 19, 20].

There are two main image reconstruction methods in MPI. The first method called the System Function Reconstruction (SFR) requires the calibration of the nanoparticle response and the imaging system, which is achieved by a time-consuming calibration scan that records the frequency response of the signal induced by the SPIOs located at all voxel locations in the FOV [21, 22, 23, 24]. The alternative image reconstruction technique, x-space reconstruction, does not require any calibration as it reconstructs the image by gridding the acquired signal to the instantaneous position of the FFP [25, 26]. The resulting x-space reconstructed images show a version of the SPIO distribution blurred by the point spread function (PSF) of the imaging system. Both of these image reconstruction techniques, with their own advantages and disadvantages, map the spatial distribution of the SPIOs.

It has recently been demonstrated that different SPIO types can be distinguished via a multi-color MPI technique [27], and numerous applications have already been shown to benefit from this novel approach. One such application is catheter tracking during cardiovascular interventions [28]. In such applications, one SPIO type is injected into the blood stream for vessel visualization, while the catheter is coated with a different type of SPIO for tracking purposes. A further advancement of this technique involved simultaneous tracking and steering of the catheter tip via using the the magnetic fields in MPI [29, 30]. More recently, the temperature mapping capability of multi-color MPI has also been demonstrated [31].

Binding state of the SPIOs has been spectroscopically shown to change their relaxation behavior, as well [32]. In this regard, relaxation mapping can be used to probe cell or protein binding of SPIOs. Moreover, there have been efforts on drug delivery via nanocarriers [33], where multi-color MPI can offer additional tracking possibilities. Likewise, multi-color MPI can also be used to identify the characteristics of an environment such as viscosity and temperature, which are shown to affect the nanoparticle relaxation behavior significantly [34, 35, 36, 37, 38, 39]. These conditions can be an important tool for probing the changes in

tissue environments, e.g., in the case of hyperthermia treatments. All of the aforementioned applications create an immense room for further experimental work and research.

To date, multi-color MPI has been realized via both the SFR and the x-space approaches. In the SFR approach, SPIOs were differentiated based on the differences in their harmonic responses, which were obtained using an extensive calibration procedure performed separately for each SPIO type [27]. For the x-space approach, the relaxation behaviors of different SPIO types were distinguished by utilizing multiple measurements at different drive field amplitudes [40].

In this thesis, a novel, calibration-free multi-color MPI technique for x-space MPI is presented. This technique can generate a relaxation time constant map of SPIOs from a single scan at a single drive field amplitude by taking advantage of the back and forth scanning of a FOV to estimate the relaxation time directly from the MPI signal, without any a priori knowledge about the SPIOs. The proposed technique is demonstrated with simulation results, MPS experiments, and imaging experiments. The results show that the proposed method successfully distinguishes multiple SPIO types, without requiring any calibrations.

Chapter 2

Background and Theory

2.1 Magnetic Particle Imaging Physics

2.1.1 Spatial Encoding

Magnetic Particle Imaging (MPI) utilizes the nonlinear magnetization curves of SPIOs for both spatial encoding and signal acquisition purposes. This nonlinear magnetization is modeled by a Langevin function, shown in Fig. 2.1, where SPIOs saturate above a certain threshold of external magnetic field.

When the SPIOs are saturated, they cannot react to the small changes in the external magnetization. This saturation property is exploited to enable spatial encoding by applying an inhomogeneous selection field that saturates the SPIOs in the entire imaging volume except for a small region. In a generic MPI scanner topology, this selection field is obtained by placing two strong magnets so that their north poles face each other, as shown in Fig. 2.2a. Here, magnetic fields originated from the two magnets, indicated with blue curves, cancel each other out in the center of the scanner to create a field-free point (FFP). Then, an oscillating, or specifically a sinusoidal, drive field is superimposed to the selection field. Saturated SPIOs cannot react to this drive field, whereas SPIOs that are in

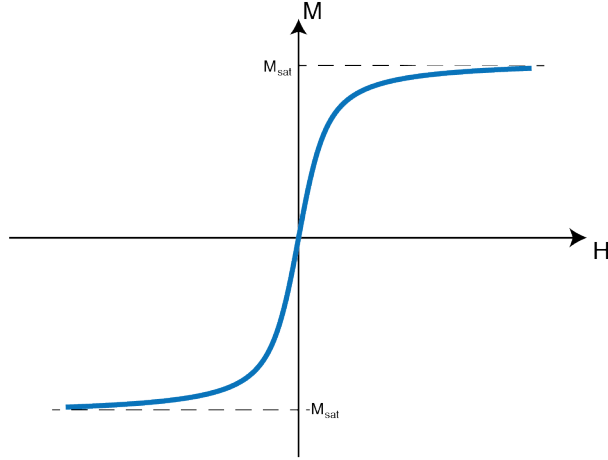


Figure 2.1: Nonlinear magnetization curve of SPIOs. Horizontal axis (H) shows the external magnetic field, vertical axis (M) shows the SPIO magnetization. M_{sat} denotes the saturation magnetization of SPIOs.

the FFP experience a time-varying magnetization change, which induces a signal on an inductive receive coil. The saturated and unsaturated SPIO responses are shown in Fig. 2.2b.

As Fig. 2.2 clearly depicts, in such an MPI scanner topology, signal that is acquired with the receive coil is induced only by the SPIOs inside or near the FFP. The overall imaging volume can then be scanned by steering the FFP in 3D via drive and/or focus fields. Since the position of the FFP is controlled at all times, this MPI scanner topology enables the spatial encoding of the acquired signals.

2.1.2 1D MPI Signal Equation

1D MPI signal equation can be derived by investigating the effects of the selection and drive fields on the SPIO magnetization. A 1D selection field can be written in the following form:

$$H_s(x) = -G \cdot x \quad (2.1)$$

where, $H_s(x)$ [T] is the selection field as a function of space, $-G$ [T/m/ μ_0] is the gradient of the selection field, and x [m] is the spatial position. Solving $H_s(x) = 0$

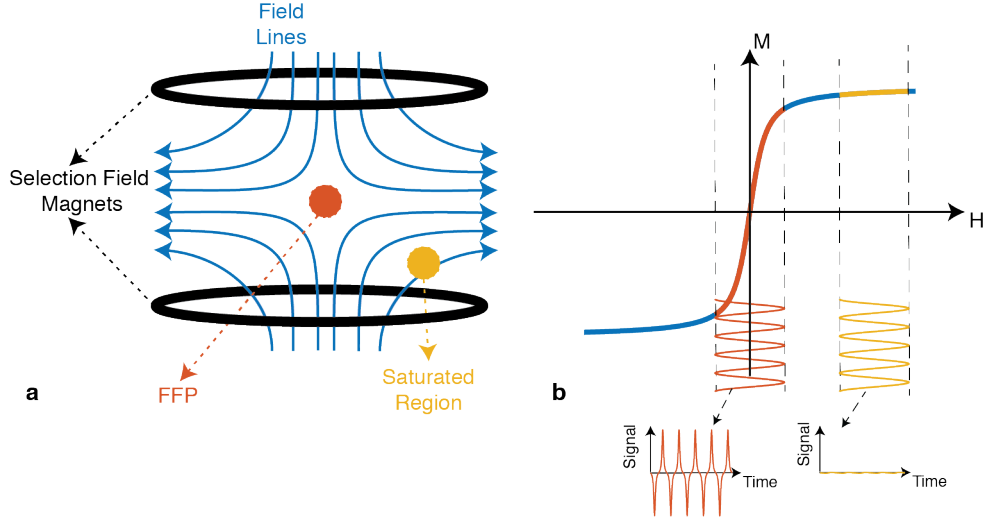


Figure 2.2: (a) Topology of an MPI scanner, where black circles denote selection field coils. Here, blue arrows denote the magnetic field lines and their directions. Orange dot denotes the FFP, while yellow dot denotes a region where the SPIOs are saturated by the selection field. (b) Comparison of signals acquired from SPIOs that are unsaturated (orange) and saturated (yellow) by the selection field. Here, orange and yellow regions experience the same sinusoidal drive field, with a different selection field component. When particles are not saturated, they induce a signal on the receive coil (orange plots). When the particles are saturated, they cannot react to the sinusoidal drive field and cannot induce a signal on the receive coil (yellow plots).

for a non-zero gradient yields the spatial position of the FFP, which is $x = 0$ in the absence of additional fields. Next, a sinusoidal drive field is superimposed to the selection field to excite the SPIOs. The overall magnetic field can be written as follows:

$$\begin{aligned}
 H(x, t) &= H_s(x) + H_d(t) \\
 &= -G \cdot x + H_{peak} \cdot \cos(2\pi f_d t)
 \end{aligned}
 \tag{2.2}$$

Here, $H_d(t)$ is the sinusoidal drive field, $H_{peak}[T]$ is the peak amplitude of the drive field, and $f_d[Hz]$ is the frequency of the drive field. In the presence of a drive field, one can find the location of the FFP by solving $H(x, t) = 0$ equation

for x , i.e., x :

$$H(x) = -G \cdot x + H_d(t) = 0 \quad (2.3)$$

$$H_d(t) = G \cdot x_s(t) \quad (2.4)$$

$$x_s(t) = \frac{H_d(t)}{G} = \frac{H_{peak} \cdot \cos(2\pi f_d t)}{G} \quad (2.5)$$

Equation 2.5 denotes the instantaneous position of the FFP. Here, $x_s(t)[m]$ denotes the FFP position in the presence of a drive field. As stated in Section 2.1.1, magnetization M of the SPIOs in the presence of an external magnetic field, H , can be expressed as follows:

$$M = m\rho\mathcal{L}[kH] \quad (2.6)$$

Here, m [Am^2] is the magnetic moment of the nanoparticles, ρ [particles/ m^3] is nanoparticle density, k [m/A] is a nanoparticle property defined as the inverse of the field required for saturation, and $\mathcal{L}[\cdot]$ is the Langevin function. Substituting Eq. 2.5 into Eq. 2.6, and assuming the nanoparticle density is 1D function, one can derive the magnetization of SPIOs as a function of space and time [25]:

$$M(x, t) = m\rho(x)\delta(y)\delta(z)\mathcal{L}[kG(x_s(t) - x)] \quad (2.7)$$

Here, SPIO density is assumed to exist only along the x-direction. One can then convert the magnetization to a 1D flux [25]:

$$\begin{aligned} \Phi(t) &= -m \iiint \rho(u)\delta(v)\delta(w)\mathcal{L}[kG(x_s(t) - u)] du dv dw \\ &= -m\rho(x) * \mathcal{L}[kGx]|_{x=x_s(t)} \end{aligned} \quad (2.8)$$

Since the MPI signal is collected with an inductive detector, i.e. a receive coil, the MPI signal equation can be expressed as the temporal derivative of the magnetic flux [25]:

$$s_{adiab}(t) = -B_1 \frac{d\Phi(t)}{dt} = B_1 m\rho(x) * \dot{\mathcal{L}}[kGx]|_{x=x_s(t)} kG\dot{x}_s(t) \quad (2.9)$$

Here, B_1 [T/A] is the receive coil sensitivity, $\dot{x}_s(t)$ [m/s] is the FFP velocity, and $\dot{\mathcal{L}}[\cdot]$ is the derivative of the Langevin function [25].

2.1.3 SPIO Relaxation

Equation 2.9 defines the MPI signal with the assumption that the SPIOs react to the drive field instantaneously. However, in practice, a delay process called relaxation takes place. Under an oscillating drive field, for particles around 25 nm, two separate relaxation mechanisms simultaneously occur [41]: in Neel relaxation, SPIOs change the orientation of their magnetic moment internally, whereas in Brownian relaxation, SPIOs physically rotate in order to align their magnetic moment with the changing external magnetic field. These two relaxation processes occur in parallel. In the end, the relaxation causes a widening, lagging and an SNR loss in the MPI signal. Figure 2.3 demonstrates the Brownian and Neel relaxations, and the effect of relaxation on the MPI signal.

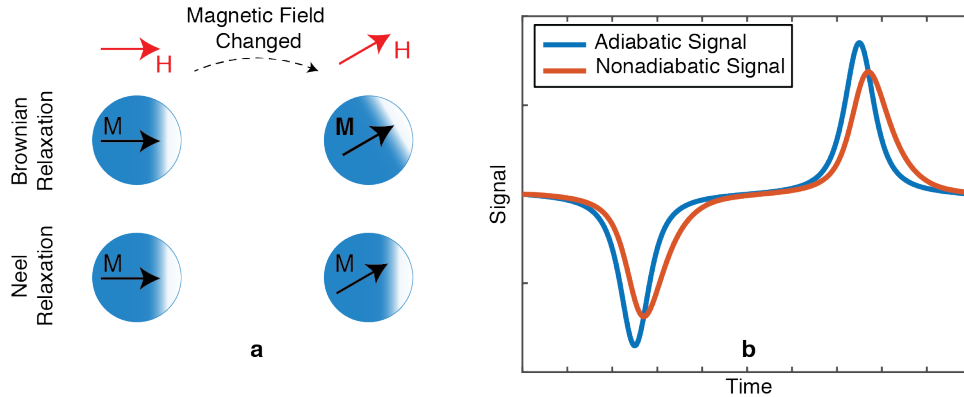


Figure 2.3: (a) Illustration of Brownian and Neel relaxations. Initially magnetic moments of the SPIOs are aligned with the horizontal external magnetic field. When external magnetic field is rotated, SPIOs physically rotate to align their magnetization via the Brownian relaxation process, and/or SPIOs change the direction of their magnetic moments internally via the Neel relaxation process. (b) MPI signal with and without relaxation. Here adiabatic signal denotes the MPI signal without relaxation, and nonadiabatic signal denotes the MPI signal with relaxation. Due to the relaxation effects, the MPI signal lags (peak of the signal shifts in time), widens, and loses SNR (peak amplitude of the signal decreases).

The nanoparticle relaxation can be mathematically modelled as a first-order Debye process, which can be modeled as a temporal convolution of the adiabatic

MPI signal with an exponential relaxation kernel [42]:

$$s(t) = s_{adiab}(t) * r(t) \quad (2.10)$$

$$r(t) = \frac{1}{\tau} e^{-\frac{t}{\tau}} u(t) \quad (2.11)$$

Here, $r(t)$ denotes the relaxation kernel, $u(t)$ is the Heaviside step function, and τ is the relaxation time constant. The resulting MPI signal, $s(t)$, is called the non-adiabatic signal. Via extensive experimental studies, this simple yet powerful model has been shown to accurately match the relaxation effect for a wide range of drive field frequencies and amplitudes [42, 43].

2.2 Image Reconstruction Methods

There are two main image reconstruction methods in MPI: System Function Reconstruction (SFR) and X-space Reconstruction.

2.2.1 System Function Reconstruction

SFR method first records the impulse response of the imaging system by acquiring extensive calibration measurements of point-like sources at all pixel locations inside the FOV. After collecting the calibration measurements, a system matrix is formed, which corresponds to the impulse response of the overall MPI system in Fourier domain, acquired at all pixel location. Figure 2.4 summarizes the calibration procedure for a 2D case [21, 22, 23, 24].

Once the system matrix is obtained, an MPI image can be reconstructed by solving the following inverse problem:

$$S \cdot c = u \quad (2.12)$$

Here, S is the system matrix, c is the reconstructed MPI image, and u is the acquired MPI signal corresponding to the image c . SFR method solves Eq. 2.12

for c to reconstruct the MPI image. Here, it is important to note that the resulting MPI image is not blurred by the PSF of the MPI system, because the inverse solution of Eq. 2.12 corresponds to an inherent deconvolution in the image domain with the PSF of the imaging system.

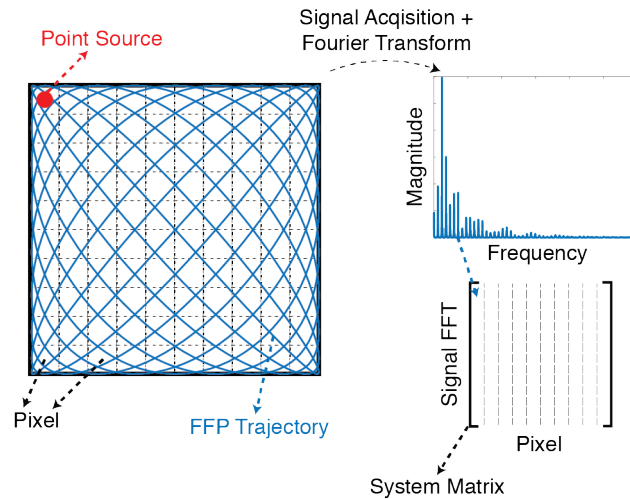


Figure 2.4: Illustration of calibration measurement for SFR. Here, calibration for one pixel location is illustrated. Red dot denotes a point source that is used for calibration. Blue curve denotes the FFP trajectory that scans the entire FOV. Once the signal is acquired with this FFP trajectory, Fourier transform of this measurement is recorded to the a column of the system matrix. Each column in the system matrix corresponds to a calibration measurement from one pixel. Overall calibration procedure includes the calibration measurements for every pixel in the FOV.

2.2.2 X-space Reconstruction

Inspired by magnetic resonance imaging (MRI) image reconstruction techniques, the X-space reconstruction grids the acquired MPI signal to the instantaneous position of the FFP [25, 26]. Since there is no deconvolution involved in the image reconstruction, a calibration measurement is not needed in x-space reconstruction. However, images reconstructed with the x-space method show a blurring caused by the PSF of the imaging system. Starting from the 1D MPI signal, in Eq. 2.9,

the image equation can be expressed as follows [25, 26]:

$$\begin{aligned} IMG(x_s(t)) &= \frac{s_{adiab}(t)}{B_1 m k G \dot{x}_s(t)} \\ &= \rho(x) * \dot{\mathcal{L}}[kGx]|_{x=x_s(t)} \end{aligned} \quad (2.13)$$

Here, $\dot{\mathcal{L}}[\cdot]$ is the 1D PSF of the MPI system, and division with the $\dot{x}_s(t)$ [m] is called velocity compensation. Note that Eq. 2.13 formulates the x-space MPI image for the adiabatic (without relaxation) signal. When the relaxation effect is incorporated, the MPI images show an SNR loss and an additional blurring along the scanning direction. Multidimensional PSF of the MPI system can be derived utilizing similar physical concepts as in the 1D PSF [25]. Figure 2.5 displays a multidimensional example for the x-space reconstruction, where Fig. 2.5a is the SPIO distribution in a FOV, Fig. 2.5b is the multidimensional PSF, and Fig. 2.5c is the x-space MPI image. Here, the blurring in the MPI image is anisotropic, i.e., it is less severe along the scanning direction (left-right in the image) and more pronounced along the other direction. It is important to note that, the x-space image reconstruction scheme (i. e., velocity compensation and gridding) remains the same for the multidimensional case.

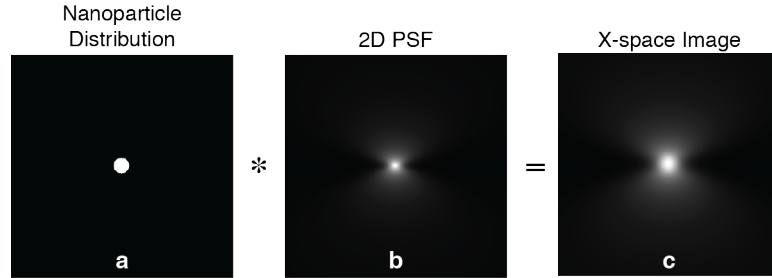


Figure 2.5: Illustration of X-space Reconstruction. (a) An example circular SPIO distribution. (b) Multidimensional PSF of the MPI system. (c) Image obtained with the x-space reconstruction. The resulting image shows the SPIO distribution blurred by the PSF of the system.

2.3 Multi-color Magnetic Particle Imaging

MPI maps the spatial distribution of the SPIOs in a FOV. Therefore MPI images are sensitive to the quantity of the SPIOs, however, it lacks the SPIO-type or environment based contrast that enables functional imaging. Recently, multi-color MPI techniques that are capable of distinguishing different SPIO types were proposed. To date, multi-color MPI has been realized via both the SFR and the x-space approaches.

In the SFR approach, SPIOs and environmental conditions (i. e., temperature, viscosity, etc.) are differentiated based on the differences in the harmonic responses to the applied selection field and drive field. To achieve an accurate differentiation, however, SFR approach requires an extensive calibration procedure for every SPIO type and environmental condition that is desired to be differentiated [31, 39]. After required calibration measurements are collected, multi-color MPI image is obtained by solving a modified version of Eq. 2.12 [27]:

$$\begin{bmatrix} S_1 & S_2 & S_3 \end{bmatrix} \cdot \begin{bmatrix} c_1 \\ c_2 \\ c_3 \end{bmatrix} = u \quad (2.14)$$

Here, S_1 , S_2 , and S_3 are different system matrices corresponding to, for example, different SPIO types. If Eq. 2.14 is solved for c_1 , c_2 and c_3 , separate images of different SPIO types can be obtained. Later, a multi-color image can be reconstructed by assigning different colors to c_1 , c_2 and c_3 and combining the colored images [27].

The x-space approach, on the other hand, differentiates the SPIOs based on the changes in their response when different drive field amplitudes are applied. To achieve the SPIO differentiation, first, calibration measurements at multiple drive field amplitudes are obtained for each SPIO type or environment. Later, image is acquired at the same drive field amplitudes and a pixel-wise inverse problem is solved to differentiate SPIO types and environmental conditions [40].

Both of these methods, have been demonstrated via experimental studies.

However, they either require an extensive calibration procedure for every condition that is desired to be distinguished, or an image acquisition at multiple drive field amplitudes. This thesis proposes a method to distinguish the nanoparticles based on their relaxation responses, without any need for a calibration scan or multiple images acquired at different field amplitudes.

Chapter 3

Direct Relaxation Time Constant Estimation

This chapter is based on the publication titled “Calibration-Free Relaxation-Based Multi-Color Magnetic Particle Imaging”, Y. Muslu, M. Utkur, O.B. Demirel, E.U. Saritas, posted on arXiv.org (2017).

3.1 Theory

In MPI, a sinusoidal drive field is applied to excite the SPIOs, while additional focus fields are applied to control the global position of the FFP. For a fixed focus field amplitude, the resulting FFP trajectory scans a partial field-of-view (pFOV) back and forth around a central position. For simplicity, the forward motion of the FFP is called the positive scan, while the backward motion is called the negative scan. In Fig. 3.1a-b, a ramp-shaped SPIO density and the corresponding MPI image are given. For the back and forth trajectory, one would expect the signals acquired during these two scans to be mirror symmetric or point symmetric (i.e., symmetric with respect to the central time point of one period), as displayed in Fig. 3.1c-d. However, the nanoparticle relaxation causes an asymmetric blurring

that breaks the mirror symmetry, as shown in Fig.3.1e.

Underlying mirror symmetry of the adiabatic signal can be used to directly estimate the relaxation time constant from the MPI signal [38, 44, 45]. In this technique, the effects of relaxation are formulated in Fourier domain. Accordingly, $s_{\text{pos}}(t)$ is defined as the signal acquired during the positive scan, and $s_{\text{neg}}(t)$ defined as the signal acquired during the negative scan, both centered with respect to time. For the adiabatic MPI signal, $s_{\text{pos,adiab}}(t)$ and $s_{\text{neg,adiab}}(t)$ are mirror symmetric, i.e.,

$$s_{\text{pos,adiab}}(t) = -s_{\text{neg,adiab}}(-t) = s_{\text{half}}(t) \quad (3.1)$$

where, $s_{\text{half}}(t)$ denotes half a period of the adiabatic MPI signal. Using the relaxation formulation in Eq. 2.10, the non-adiabatic positive and negative signals can be expressed as:

$$s_{\text{pos}}(t) = s_{\text{pos,adiab}}(t) * r(t) = s_{\text{half}}(t) * r(t) \quad (3.2)$$

$$s_{\text{neg}}(t) = s_{\text{neg,adiab}}(t) * r(t) = -s_{\text{half}}(-t) * r(t) \quad (3.3)$$

Here, $s_{\text{half}}(t)$ and $r(t)$ are the unknowns of the equations while $s_{\text{pos}}(t)$ and $s_{\text{neg}}(t)$ are measured waveforms. In Fourier domain, these equations can be expressed as:

$$\mathcal{F}\{r(t)\} = R(f) = \frac{1}{1 + i2\pi f\tau} \quad (3.4)$$

$$\mathcal{F}\{s_{\text{pos}}(t)\} = S_{\text{pos}}(f) = S_{\text{half}}(f) \cdot R(f) \quad (3.5)$$

$$\mathcal{F}\{s_{\text{neg}}(t)\} = S_{\text{neg}}(f) = -S_{\text{half}}^*(f) \cdot R(f) \quad (3.6)$$

where \mathcal{F} is the Fourier transform operator, and the time reversal and conjugate symmetry properties of Fourier Transform are used to express $S_{\text{neg}}(f)$. Using Eqs. 3.4-3.6, τ can be calculated directly as follows:

$$\tau(f) = \frac{S_{\text{pos}}^*(f) + S_{\text{neg}}(f)}{i2\pi f(S_{\text{pos}}^*(f) - S_{\text{neg}}(f))} \quad (3.7)$$

Ideally, performing this calculation at a single frequency in Fourier domain suffices. However, the accuracy of the estimation is different at each frequency component due to relative strengths of signal vs. noise. To increase the robustness of the estimation against noise, a weighted average of $\tau(f)$ is calculated with

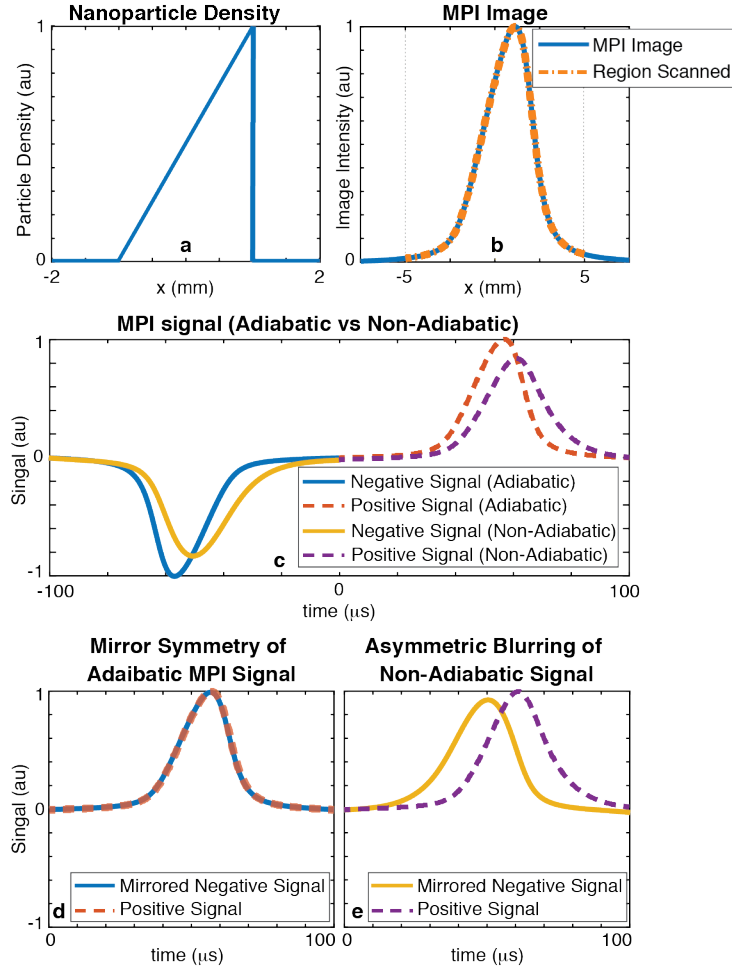


Figure 3.1: The mirror symmetry of the adiabatic MPI signal and how the relaxation effects break that mirror symmetry. (a) A ramp-shaped nanoparticle density. (b) The corresponding ideal MPI image obtained by the convolution of nanoparticle density and the point spread function. (c) Adiabatic vs. non-adiabatic MPI signals for a ramp-shaped nanoparticle density. Here, one full periods of the signals are shown (i.e., the signals from both the negative and positive cycles). (d) In the adiabatic case, due to the repetitive nature of applied sinusoidal drive field, positive and mirrored negative signals match perfectly. This phenomenon is referred as "mirror symmetry". (e) The relaxation effect causes an asymmetric blurring of the negative and positive signals, which in turn breaks the mirror symmetry.

respect to the magnitude spectrum:

$$\tau = \frac{\int_0^{f_{\max}} |S_{\text{pos}}(f)| \tau(f) df}{\int_0^{f_{\max}} |S_{\text{pos}}(f)| df} \quad (3.8)$$

Here, f_{\max} is an upper threshold for the range of frequencies used, such that $0 < f_{\max} \ll \frac{F_s}{2}$, where F_s is the sampling frequency. Typically, including frequencies up to 6th or 7th harmonic of the fundamental frequency suffices, as the signal falls off rapidly with increasing frequency.

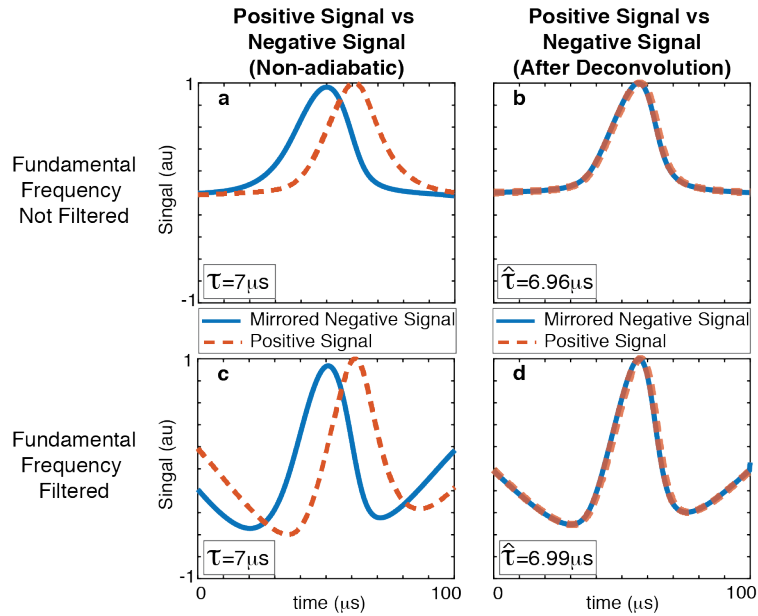


Figure 3.2: The proposed method: direct relaxation time constant estimation. (a) The mirror symmetry between the positive and negative signals is broken due to relaxation. The proposed method estimated $\hat{\tau} = 6.96 \mu\text{s}$, where $\tau = 7 \mu\text{s}$ in theory. (b) MPI signal is then deconvolved with the estimated relaxation kernel using $\hat{\tau} = 6.96 \mu\text{s}$, which recovers the underlying mirror symmetry. Here, (a, b) demonstrate the case where the fundamental frequency is kept intact in simulations, and (c, d) demonstrate the case after direct feedthrough filtering that removes the fundamental frequency. In the latter case, the estimation resulted in $\hat{\tau} = 6.99 \mu\text{s}$.

The direct relaxation time constant estimation method is tested in MATLAB (Mathworks, Natick, MA). Figure 3.2 demonstrates the proposed relaxation time constant estimation method on a simulated MPI signal. Here, the same ramp-shaped nanoparticle density in Fig. 3.1a is assumed and a central pFOV is scanned to obtain the MPI signal. Simulation parameters were as follows: 15 mT-peak

drive field at 5 kHz, 3 T/m/ μ_0 gradient, 2 Ms/s sampling frequency, 21 nm nanoparticle diameter, and 7 μ s relaxation time constant. First, the MPI signal is simulated using a very small discretization time step of 1 ns. The relaxation effect is then incorporated via the exponential model in Eq. 2.10. Next, this MPI signal is resampled with the sampling frequency of our data acquisition card (2 Ms/s) to ensure that the results are realistic.

For the MPI signal with the fundamental frequency, the estimated time constant yielded $\hat{\tau} = 6.96 \mu$ s. The signal was then deconvolved using the estimated relaxation kernel, recovering the underlying mirror symmetry (see Fig. 3.2a-b). The same procedure was repeated on the MPI signal after direct feedthrough filtering [46, 47], to ensure that the filtering of the fundamental harmonic (a necessary step in MPI) does not hinder the performance of the proposed technique, where the estimated time constant yielded $\hat{\tau} = 6.99 \mu$ s (see Fig. 3.2c-d). In the absence of noise in both cases, the proposed method estimated τ with less than 0.6% error. This error increases for larger discretization time steps (e.g., 2% error for 20 ns) and steadily converges to zero for smaller time steps. Hence, it is concluded that this error is primarily caused by the discretization in simulating the relaxation effect via convolution.

3.2 Simultaneous Hardware Delay and Relaxation Time Constant Estimation

Finding the correct time intervals for $s_{\text{pos}}(t)$ and $s_{\text{neg}}(t)$ is crucial for the proposed relaxation time estimation method. In simulations, this procedure is trivial since the timing of the signal vs. the FFP trajectory (i.e., the time point, t_{edge} , when the positive scan ends and the negative scan starts) is known. In practice, however, system delays introduce a time shift between the signal vs. the FFP trajectory. In such cases, incorrect t_{edge} values introduce extra phase terms in Eq. 3.7 (see Appendix C), causing incorrect estimation of τ . One method for measuring t_{edge} is performing a calibration scan with an SPIO that exhibits negligible relaxation

(e.g., fluidMAG nanoparticles by Chemicell, as suggested in [42]). Here, a novel procedure that estimates the correct τ and t_{edge} simultaneously is proposed, eliminating the need for a fine-tuned calibration scan.

Equation 3.1 argues that deconvolution of the MPI signal with the correct relaxation kernel should restore mirror symmetry. Here, this phenomenon is exploited to simultaneously find the correct τ and t_{edge} , as outlined in Fig. 3.3. First, a t_{edge} value is chosen, τ is estimated directly using Eq. 3.8, and MPI signal is deconvolved with the estimated relaxation kernel. This step is then repeated for a range of t_{edge} values limited to $[0, T/2)$ region of the MPI signal, where T is the drive field period. The correct pair, $(\hat{\tau}, \hat{t}_{\text{edge}})$, should restore the mirror symmetry, minimizing the mean squared error (MSE) between positive and mirrored negative signals after deconvolution, i.e.,

$$(\hat{\tau}, \hat{t}_{\text{edge}}) = \underset{(\tau, t_{\text{edge}})}{\operatorname{argmin}} \int_0^{T/2} (\hat{s}_{\text{pos}}(t) - (-\hat{s}_{\text{neg}}(-t)))^2 dt \quad (3.9)$$

where $\hat{s}_{\text{pos}}(t)$ and $\hat{s}_{\text{neg}}(t)$ depend on τ and t_{edge} , and denote the signals after deconvolution with the estimated relaxation kernel. A detailed analysis showing that Eq. 3.9 has a unique minimum is given in Appendix C. Here, instead of computing MSE over the entire half period, more weights can be assigned to central time points that typically have higher signal-to-noise ratio (SNR) [38]. In addition, the search for t_{edge} could also be performed in $(-T/2, 0]$, which would yield an identical $\hat{\tau}$ value.

3.3 Magnetic Particle Spectrometer Experiments

3.3.1 MPS Setup

The initial experiments of the proposed relaxation time estimation method were conducted on our in-house MPS (also known as MPI Relaxometer) setup. The

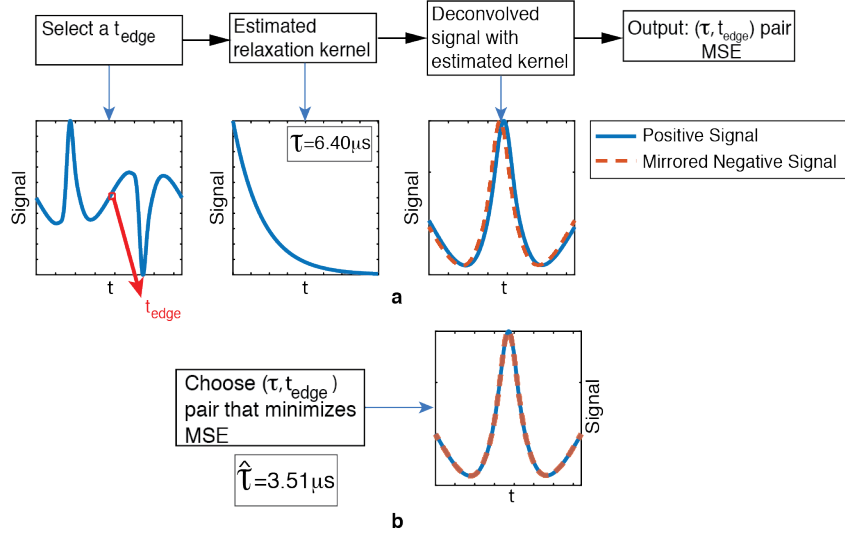


Figure 3.3: Experimental relaxation time constant estimation algorithm. (a) A time point t_{edge} is chosen to mark the time when positive scan finishes and negative scan starts. Then, τ is estimated for different t_{edge} values chosen from $[0, T/2)$ interval. The MSE between the deconvolved positive and mirrored negative signals are computed for each case. (b) The MSE values are compared, and the (τ, t_{edge}) pair that minimizes MSE is chosen as the solution. For this example, the result is $\hat{\tau} = 3.51 \mu\text{s}$. Here, the black arrows show the flow of the algorithm, while blue arrows show a visual demonstration of each step.

drive coil of the relaxometer produces 0.97 mT/A magnetic field with 95% homogeneity in a 7 cm long region. The receive coil of the relaxometer was designed as a three-section gradiometer pick-up coil [38], to minimize the direct feedthrough signal. A more detailed explanation of the setup can be found in [38].

Experiments were conducted at 10.8 kHz and 15 mT-peak drive field. The nanoparticle signal was first amplified with a low-noise voltage preamplifier (Stanford Research Systems SR560), then digitized at 2 MS/s via a data acquisition card (National Instruments, NI USB-6363). 16 consecutive signal acquisitions were performed, each with 30 ms drive field pulse duration. Received signals were averaged, providing a 4-fold SNR improvement. A background measurement was subtracted from the averaged signal to minimize the effects of potential background interferences in the higher harmonics of the fundamental frequency. A frequency domain filter was applied by selecting the higher harmonics of the

drive field and setting the rest of the frequency components to zero in Fourier domain. Next, a high-order zero-phase digital low pass filter (LPF) was applied in time domain to avoid ringing artifacts. The cut-off frequency of the LPF was determined by setting an SNR threshold of 2 in the frequency domain, and avoiding the 250 kHz self-resonance frequency of the receive coil, which corresponded to a cut-off frequency of 180 kHz. For the deconvolution step of the proposed method, Wiener deconvolution is used and a relatively large noise to signal power ratio of 100 is chosen to prevent noise amplification.

3.3.2 Sample Preparation

For MPS experiments, VivoTrax ferucarbotran nanoparticles (Magnetic Insight Inc., USA) with the same chemical composition as Resovist, and Nanomag-MIP nanoparticles (Micromod GmbH, Germany) were prepared in 25 μL volumes. The original concentrations of Nanomag-MIP and VivoTrax were 5.5 mg Fe/mL and 5 mg Fe/mL, respectively. The Nanomag-MIP sample was diluted 3.5 times to equalize its peak signal level with that of the VivoTrax sample. In addition, a 50%-50% homogeneous mixture of the two samples was prepared in 25 μL volume.

3.4 Results

Figure 3.4 presents the experimental validation for the proposed relaxation time constant estimation technique. Figure 3.4a and 3.4c show the non-adiabatic MPI signals obtained from Nanomag-MIP and VivoTrax SPIOs, respectively. The τ values for Nanomag-MIP and VivoTrax SPIOs were estimated as 3.28 μs and 4.46 μs , respectively. After the deconvolution with the estimated relaxation kernel, as shown in Fig. 3.4b and 3.4d, mirror symmetry property is recovered.

Figure 3.5 presents the experimental validation for the homogeneous mixture case, where the relaxation time constant of a homogeneous mixture of Nanomag-MIP and VivoTrax SPIOs are measured. A detailed derivation for the relaxation

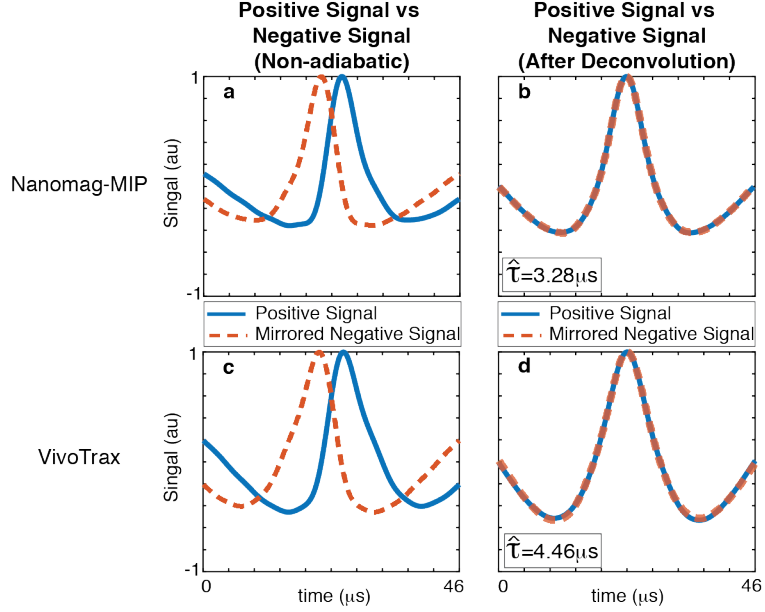


Figure 3.4: Experimental demonstration in the MPS setup. (a) Picture of our in-house MPS setup, showing the drive and receive coils placed co-axially. (b) Signal acquired from Nanomag-MIP (blue) and VivoTrax (orange) SPIOs, and their homogeneous mixture (yellow). The Nanomag-MIP and VivoTrax SPIOs yielded $\hat{\tau} = 3.28 \mu s$ and $\hat{\tau} = 4.46 \mu s$, respectively.

time constant estimation of a homogeneous mixture of two distinct nanoparticles is provided in Appendix A. According to this derivation, the proposed technique can be used to determine the relative concentrations of the constituents in a homogeneous mixture. Since the MPS signal levels of the SPIOs were equalized beforehand, the expected τ for the homogeneous mixture was equal to $3.87 \mu s$, i.e., the average of the τ values for Nanomag-MIP and VivoTrax. The estimation revealed a relaxation time of $3.89 \mu s$, closely matching the expected value.

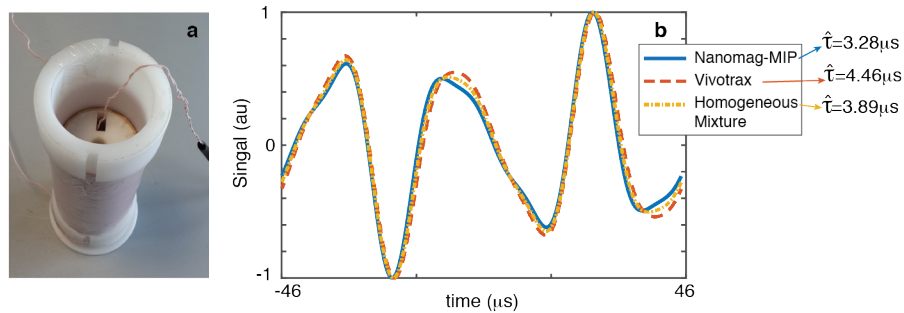


Figure 3.5: Experimental demonstration of the homogeneous mixture case in the MPS setup. (a) Picture of our in-house MPS setup, showing the drive and receive coils placed co-axially. (b) Signal acquired from Nanomag-MIP (blue) and VivoTrax (orange) SPIOs, and their homogeneous mixture (yellow). The Nanomag-MIP and VivoTrax SPIOs yielded $\hat{\tau} = 3.28 \mu\text{s}$ and $\hat{\tau} = 4.46 \mu\text{s}$, respectively. The homogeneous mixture gave $\hat{\tau} = 3.89 \mu\text{s}$, closely matching the expected value of $3.87 \mu\text{s}$ based on the average of the Nanomag-MIP and VivoTrax relaxation times.

Chapter 4

Calibration-Free Multi-Color MPI

This chapter is based on the publication titled “Calibration-Free Relaxation-Based Multi-Color Magnetic Particle Imaging”, Y. Muslu, M. Utkur, O.B. Demirel, E.U. Saritas, posted on arXiv.org (2017).

4.1 Algorithm

For the proposed multi-color MPI technique, a relaxation time constant for each pFOV is directly estimated, and the estimated time constant is mapped to the central position of the pFOV. While this mapping sounds simple at first, extensive simulations revealed two special cases where the additional steps are needed for accurate mapping of time constants:

1. *Flat Nanoparticle Distribution:* If the nanoparticle distribution is flat in a pFOV, most of the signal is contained in the lost 1st harmonic. Hence, direct feedthrough filtering removes almost all signal, making flat regions appear like regions devoid of nanoparticles. In the absence of signal, proposed

estimation method produces noise-like results.

2. *Inhomogeneous Mixtures of Different Nanoparticle*: In the regions where two different nanoparticle types mix homogeneously, the estimation yields a weighted average of two relaxation time constants (see Appendix). However, in the case of an inhomogeneous mixture (e.g., a transition region from one nanoparticle type to the other), the adiabatic signal from each nanoparticle not only has a different shape, but is also convolved with a different relaxation kernel. Therefore, the set of equations derived in Eqs. 3.5-3.6 become underdetermined, producing noise-like estimations.

Here, these special cases are, first, detected and isolated, rest of the relaxation map is reconstructed, and finally missing portions of the map are restored. The following steps summarize the proposed multi-color MPI algorithm, outlined in Fig. 4.1 for an example case of *Inhomogeneous Mixtures*:

Phase 0 - Estimation of τ for Each pFOV: Using Eq. 3.9, algorithm directly estimates the corresponding $(\hat{\tau}, \hat{t}_{\text{edge}})$ pair for each pFOV. An x-space MPI image is reconstructed (Fig. 4.1b), and the signal root mean squared (RMS) values for pFOVs are calculated using all samples from one period of the corresponding signals (Fig. 4.1c).

Phase 1 - Histogram Correction: Using the histogram of estimated τ values from all pFOVs, a mild thresholding is applied to remove erroneous estimations. The histogram correction consists of 2 steps (see Fig. 4.1d-e):

- Upper limit on estimations: Extensive experimental work showed that τ values are smaller than 10% of the drive field period for the exponential model [43, 38]. Here, as a safe upper limit, estimations that are larger than one-fourth of the period are ignored.
- Signal RMS threshold: Low signal leads to inaccurate τ estimations. Here, estimations from low RMS regions (e.g., less than 10% of the maximum RMS value) are initially ignored.

Phase 2 - Cluster Detection: At the end of Phase 1, erroneous estimations have

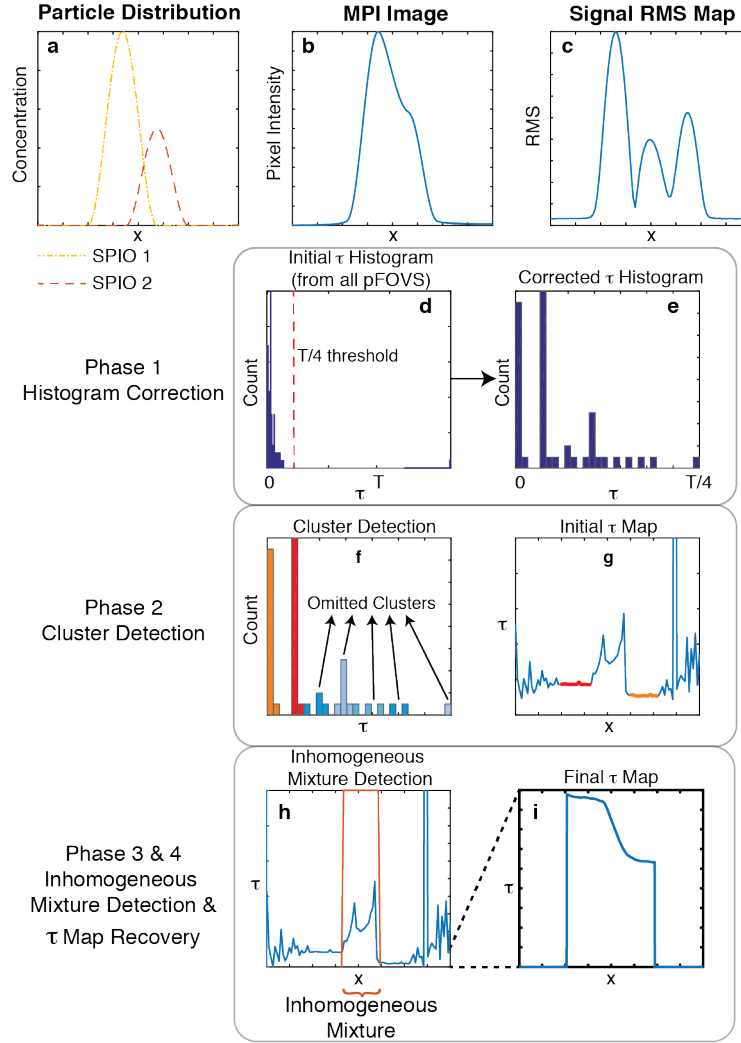


Figure 4.1: The proposed relaxation mapping algorithm. (a) The simulated particle distributions for two different SPIO types, which overlap in a small region in 1D space. (b) The x -space reconstructed MPI image. (c) Signal RMS values for each pFOV. (d) The initial relaxation time constant estimations are plotted as a histogram, and (e) the histogram is corrected by eliminating low SNR regions and overestimations (i.e., an upper threshold set at $T/4$). (f) A k -means clustering detects two main clusters (shown in orange and red). (g) These regions are highlighted in the initial τ map. (h) The inhomogeneous nanoparticle mixture region is detected, and (i) the final τ map is achieved via modeling the transition using a smooth sigmoid curve and setting low pixel intensity regions to zero. Note the change in y -axis scaling from (h) to (i).

been mostly removed. Accordingly, the remaining estimations must have the relaxation times of different SPIO types. Here, a k-means clustering algorithm is run on the remaining estimations [48]. Since the number of nanoparticle types is unknown, k parameter is started from a large value. The following procedure is then applied iteratively to reduce k , with the goal of representing the probable SPIO types (see Fig. 4.1f-g):

- Merger of clusters: Cluster centers that are closer than a τ_{res} value are merged. Note that τ_{res} must be sufficiently small to ensure the separation of different clusters. In our simulations, τ_{res} is selected as $T/100$.
- Omission of small clusters: Clusters that contain less than $p\%$ of the overall histogram are considered irrelevant and ignored. In our simulations, p is taken as 5.
- Convergence: If the cluster properties (number of clusters, cluster centers, etc.) remain the same for two consecutive iterations, convergence is achieved.

Note that the purpose of this step is to find the range of probable τ values for each SPIO type and eliminate outlier estimations. Individual τ variations within each SPIO type are still preserved.

Phase 3 - Special Case Detection: After Phase 2, clusters have been detected. Outlier τ values that are not in the vicinity of the clusters could indicate either one of the two special cases explained above. These cases have high pixel intensity in the MPI image despite having low signal RMS. Here, algorithm searches for the nearest spatial locations that have τ values belonging to a cluster, on either side of the problem pFOV. If incorrect estimations are caused by *inhomogeneous mixtures*, different clusters on either sides of the problem pFOVs are expected. On the other hand, *flat nanoparticle distributions* have a single cluster type around the problem pFOVs (see Fig. 4.1h).

Phase 4 - Recovery of τ Map: At the end of Phase 3, the regions of incorrect estimations are determined. These regions are recovered as follows (see Fig. 4.1i):

- For *Flat Nanoparticle Distributions*, the missing regions are recovered as a constant τ value.
- For *Inhomogeneous Mixtures*, the average signal RMS of the clusters are used to estimate the relative concentrations of the corresponding nanoparticle types. Next, a smooth transition region from one relaxation time to the other is modeled using a sigmoid function, with steepness determined via the relative concentrations.

Finally, estimations from low MPI pixel intensity regions are set to zero to remove the background in the τ map.

4.2 1D and 2D Simulations

4.2.1 Methods

All simulations were carried out using a custom MPI toolbox developed in MATLAB (Mathworks, Natick, MA). To obtain realistic results, the fundamental harmonic was filtered out [46], the relaxation time constant values were selected according to previous studies [43, 38], and smoothly-varying Hamming-window-shaped SPIO distributions were used to simulate real-life conditions. The MPI images were reconstructed using the x-space reconstruction technique [25, 26, 46].

For 1D simulations, a selection field with $3 \text{ T/m}/\mu_0$ gradient was utilized, with 10 mT-peak drive field at 10 kHz and 80% overlap between consecutive pFOVs. The nanoparticle diameter was selected as 21 nm (a conservative value given the recent developments in tailored SPIOs with larger diameter and narrower PSF [49]) to test the proposed methods under less ideal conditions. The relaxation times ranged between 1-5 μs , as recently reported in experimental studies performed around 10 kHz [38, 43]. To match experimental conditions, the simulated MPI signal was sampled at 2 MS/s sampling frequency, and additive white Gaussian noise corresponding to a peak signal SNR of 5 was added to the MPI signal.

For 3D simulations, a selection field with $(-7, 3.5, 3.5)$ T/m/ μ_0 gradient in (x, y, z) directions was utilized, based on the work in [46]. A 15 mT-peak drive field at 10 kHz and a 90% overlap along the z-direction was utilized, with all other parameters kept the same as in 1D simulations.

4.2.2 Results

Figure 4.2 displays the results of the proposed mapping algorithm for the 1D case, where each row corresponds to a different scenario: two, three, and four different types of SPIOs, respectively. The left column shows the spatial distributions of SPIOs with relaxation times ranging between 1-5 μ s. The MPI images, reconstructed via the x-space reconstruction, are displayed in the middle column. Each simulation includes a challenging case of inhomogeneous mixtures of different nanoparticle types. The right column shows the reconstructed relaxation maps (blue solid lines) and ideal relaxation maps (orange dashed lines). The ideal maps were calculated on a pixel-by-pixel basis by averaging τ values of SPIO constituents weighted by their relative pixel intensities. While utilizing only two different SPIO types is more likely in medical applications (e.g., coated catheter tip vs. blood pool in the case of cardiovascular interventions [30]), these results aim to show the full potential of the proposed method.

As seen in each row in Fig. 4.2, proposed mapping algorithm reconstructed the relaxation maps accurately, despite a relatively low SNR level of SNR=5 (see Appendix D for a detailed noise robustness analysis). The inhomogeneous mixture regions were detected successfully and the proposed sigmoid-transition model recovered those regions accurately. Furthermore, the proposed algorithm also eliminated background areas via a thresholding and edge detection step. The slight deviations from the ideal relaxation maps were due to noise, as well as the crosstalk of signals from different SPIOs due to proximity. For the results in Fig. 4.2c, the mean estimation error is well below 3%, whereas the mean error reaches 7% for the results in Fig. 4.2i where the SPIO distributions are closer to each other. Here, the 3.5- μ s SPIO was spatially disconnected from the other

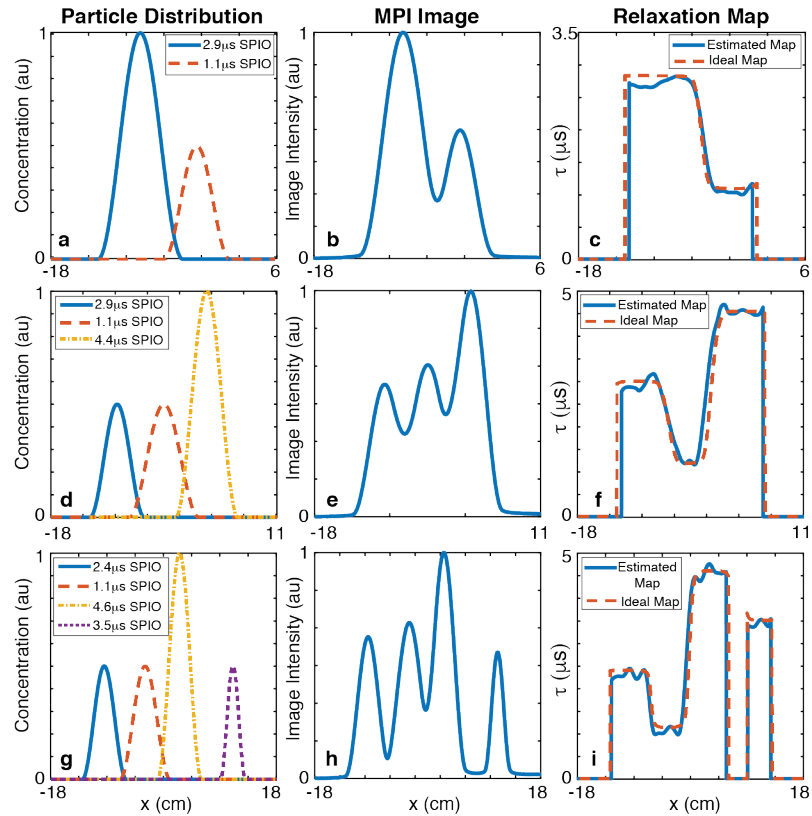


Figure 4.2: Results of 1D simulations for three different cases for SNR=5, without signal averaging. Left column (a, d, g) demonstrates the spatial distributions for different SPIOs with relaxation time constants ranging between 1-5 μs . Middle column (b, e, h) demonstrates the corresponding x-space MPI images. Right column (c, f, i) demonstrates the relaxation maps reconstructed with the proposed algorithm. The mean estimation error is well below 3% for (c), and is around 7% for (i) due to reduced distances between the different SPIO distributions.

SPIOs, which is successfully depicted in the reconstructed relaxation map.

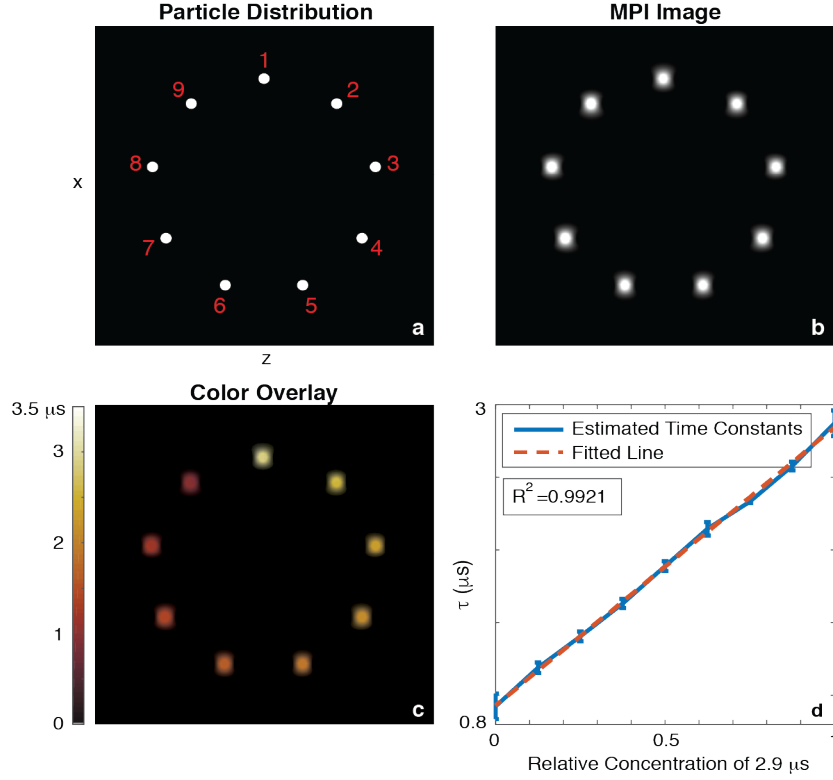


Figure 4.3: Results of 3D simulations, for SNR=5. (a) A distribution with homogeneous mixtures of $2.9 \mu\text{s}$ and $1.1 \mu\text{s}$ SPIOs in different concentrations. Each mixture is labeled with a number from 1 to 9, with concentrations of $2.9 \mu\text{s}$ SPIO in each mixture given as (100, 87.5, 75, 62.5, 50, 37.5, 25, 12.5, 0)%, respectively. (b) The x-space MPI image, and (c) the color overlay of the multi-color relaxation map and the MPI image. (d) The estimated time constants vs. relative concentrations of the two SPIOs. Here, the error bars denote the standard deviations for each ROI, and the red dashed curve is the fitted line (with $R^2 = 0.9921$). FOV size is $9 \times 9 \text{ cm}^2$. The Euclidean distance between neighboring samples is 1.7 cm.

For the multidimensional case, the proposed technique is extended in a line-by-line basis, where each line in the z-direction is reconstructed individually, then combined to form the multidimensional multi-color MPI image. In Fig. 4.3a, each SPIO distribution (labeled from 1 to 9) represents a homogeneous mixture of two different SPIOs with $2.9 \mu\text{s}$ and $1.1 \mu\text{s}$ relaxation time constants at different mixture ratios. Accordingly, the distribution labeled as 1 has 100% of $2.9\text{-}\mu\text{s}$ SPIOs, whereas the distribution labeled as 9 has 100% of $1.1\text{-}\mu\text{s}$ SPIOs. Figure

4.3b shows the resulting x-space MPI image, and Fig. 4.3c shows the relaxation map color overlay, which was obtained by multiplying the x-space MPI image and the relaxation map. In the MPI image, the regions corresponding to larger τ values resulted in slightly lower pixel intensities due to relaxation-induced signal losses. However, this difference cannot be used to distinguish the SPIOs, as lower iron concentration could also result in reduced pixel intensity. As seen in Fig. 4.3c, the proposed multi-color MPI method is capable of distinguishing a variety of SPIO types (9 in this case), each with a different time constant. Furthermore, the estimated time constants reflect the relative concentrations of the constituent SPIO types with high level of linearity ($R^2 = 0.9921$), as shown in Fig. 4.3d (see Appendix A for the detailed explanation).

4.3 Magnetic Particle Imaging Experiments

4.3.1 MPI Scanner

Our in-house MPI Scanner (see Fig. 4.4) has two disc-shaped permanent magnets with 2-cm thickness and 7-cm diameter, placed at 8-cm separation in the x-direction. The resulting configuration creates $(-4.8, 2.4, 2.4)$ T/m/ μ_0 gradient in (x, y, z) directions, which yields approximately 4-mm resolution in the z-direction (i.e., down the imaging bore) for Nanomag-MIP nanoparticles. The drive coil has 3 layers of Litz wire with 80 turns, resulting in 1.5 mT/A magnetic field with 95% homogeneity in a 4.5 cm-long region down its bore. The drive field and selection field specifications were validated using a Hall Effect Gaussmeter (LakeShore 475 DSP Gaussmeter). The receive coil was designed as a three-section gradiometer, with a single layer of Litz wire with 34 turns in the main section and 17.5 turns in the side sections. The self-resonance of the receive coil was measured at around 280 kHz. This configuration allowed 1x1x10 cm³ FOV. The drive and receive coils were placed inside a cylindrical copper shield with 1-cm thickness (to allow potential imaging applications at drive field frequencies as low as 1 kHz).

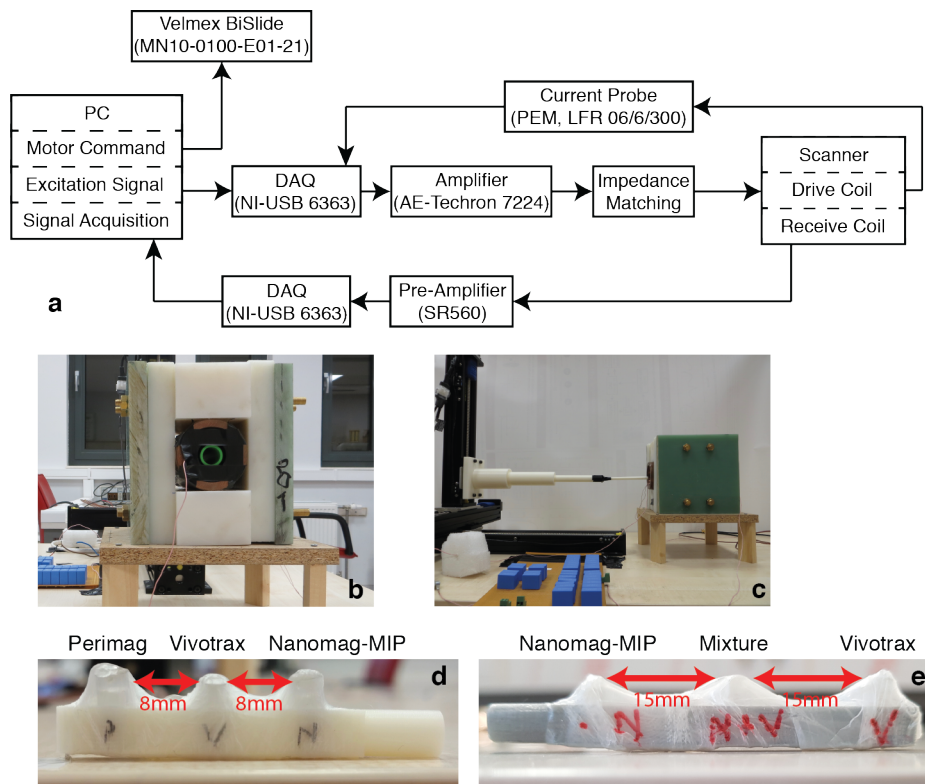


Figure 4.4: An overview of the MPI scanner and the experimental setup. (a) The entire imaging system is controlled through MATLAB, via a custom MPI imaging toolbox. First, robot position is adjusted to place the phantom at the desired location. Second, a drive field at 9.7 kHz is applied through the transmit chain, and the nanoparticle signal is simultaneously acquired through the receive chain. (b-c) Front and side views of our in-house MPI scanner. The phantoms imaged in (d) the 1D experiment and (e) the 2D experiment.

Figure 4.4a-c display the workflow of the complete MPI scanner setup, together with its front and side views. The overall imaging system was controlled via a custom toolbox implemented in MATLAB (Mathworks, Natick, MA). The drive coil was impedance matched to a power amplifier (AE Techron 7224), using a capacitive network at 9.7 kHz. The imaging phantoms were mechanically moved inside the scanner in 3D via Motor-Driven Velmex BiSlide (Model: MN10-0100-E01-21).

The drive field was at 15 mT-peak and 9.7 kHz, which resulted in a 12.5 mm pFOV length in the z-direction. The amplitude of the drive field was automatically calibrated immediately before each experiment and controlled throughout the experiment via a Rogowski current probe (LFR 06/6/300, PEM Ltd.). Partial FOVs were acquired with 85% overlaps. For the 1D imaging experiment, an 8-cm FOV along the z-direction was covered with 16.8 sec active scan time. For the 2D imaging experiment, a Cartesian trajectory was used to cover a 0.8x6.8 cm² FOV in the x-z plane using 9 lines along the z-direction, with 134 sec active scan time. The temperature inside the scanner bore was controlled throughout the experiment to prevent heating of the nanoparticles.

To boost the SNR, 16 consecutive signal acquisitions were performed, each with 30 ms drive field pulse duration. Received signals were averaged, providing a 4-fold SNR improvement. The background measurements acquired before/after each line were subtracted from the nanoparticle signal to minimize potential background interferences. All remaining signal acquisition, processing, and deconvolution steps were the same as in the MPS experiments. The MPI images were reconstructed using x-space reconstruction [25, 26, 46], followed by the proposed multi-color MPI technique.

4.3.2 Sample Preparation

Imaging phantoms with different types of SPIOs were prepared, using VivoTrax (Magnetic Insight Inc., USA), and Perimag and Nanomag-MIP nanoparticles (Micromod GmbH, Germany). These nanoparticles had original concentration levels

of 5.5 mg Fe/mL, 17 mg Fe/mL, and 5 mg Fe/mL, respectively. Perimag and Nanomag-MIP SPIOs were diluted 10.2 and 3.5 times, respectively, to approximately equalize their MPS signal levels to that of VivoTrax. This equalization was performed solely for visual reasons: to have comparable pixel intensities from these nanoparticles in the x-space MPI image. Capillary tubes with 2 mm inner diameter were filled with 10 μ L volume of SPIOs each. These tubes were then placed in custom-designed 3D-printed phantom holders in two different configurations, as shown in Fig. 4.4d-e.

4.3.3 Results

Figure 4.5 displays the 1D imaging results of the proposed technique. In this experiment, a phantom with 3 tubes, each containing a different type of SPIO was imaged. To enable color display, reconstructed 1D x-space MPI image and the 1D relaxation map were replicated and stacked vertically in a pseudo-2D image format. Figure 4.5a shows the reconstructed MPI image. Although the SPIOs were placed in identical tubes, VivoTrax covers a wider region (7.3 mm) in the MPI image, denoting a lower resolution capability. On the other hand, Perimag and Nanomag-MIP SPIOs display comparable widths (5 mm vs. 5.2 mm).

While there are differences between MPI responses of these SPIOs, it is not possible to distinguish the SPIO types based on the MPI image in Fig. 4.5a. Figure 4.5b shows the relaxation map reconstructed with the proposed algorithm. Here, different SPIO types can be clearly distinguished after color assignment. On average, Nanomag-MIP, Perimag, and VivoTrax SPIOs yielded 2.67 μ s, 3.02 μ s, and 4.15 μ s relaxation time constants, respectively. Finally, Fig. 4.5c shows the color overlay image, containing the spatial and quantitative information from both the MPI image and the relaxation map.

Figure 4.6 displays 2D experimental demonstration of the proposed method. Here, Nanomag-MIP and VivoTrax SPIOs, and their homogeneous mixture were imaged with a 15 mm separation. Again, while the two SPIOs were placed in

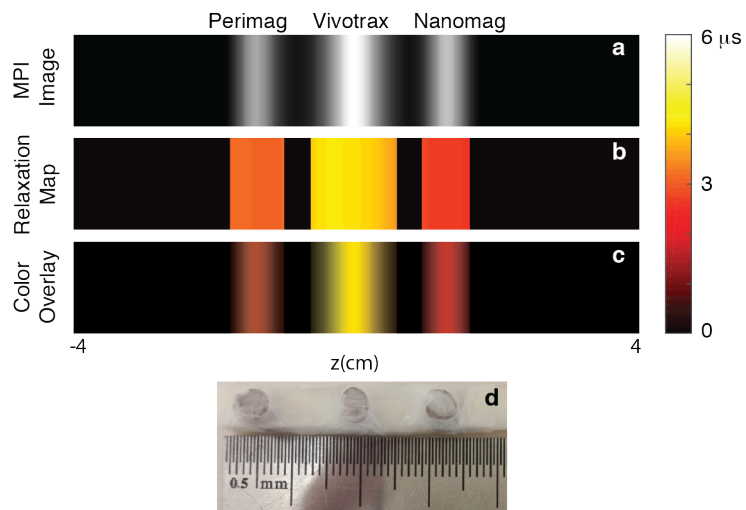


Figure 4.5: Calibration-free multi-color MPI results in 1D. The imaging experiment was conducted at 9.7 kHz and 15 mT-peak drive field, using three different nanoparticles. (a) 1D reconstructed x-space MPI image, and (b) the corresponding multi-color relaxation map. (c) The color overlay of the MPI image and the multi-color map shows that the nanoparticles can be clearly distinguished based on their relaxation responses. (d) A photo of the imaged phantom with three tubes containing Perimag, VivoTrax and Nanomag-MIP SPIOs from left to right, separated at 8mm distances.

identical tubes, VivoTrax displays a significantly wider PSF in both x- and z-directions in the MPI image in Fig. 4.6a. Accordingly, the homogeneous mixture shows less blurring than VivoTrax but larger blurring than Nanomag-MIP. In both the relaxation map and the color overlay image, Nanomag-MIP and VivoTrax SPIOs, and their homogeneous mixture can be distinguished clearly. The average time constants were measured as $3.97 \mu\text{s}$, $3.57 \mu\text{s}$ and $2.82 \mu\text{s}$ respectively. Here, due to the differences in the SPIO responses under a gradient field, MPI signal ratio of VivoTrax to Nanomag-MIP was 1.6:1. Considering this signal ratio, the expected relaxation time constant of the homogeneous mixture was $3.53 \mu\text{s}$, which closely matches the experimental result.

In Fig. 4.6b, at the peripheries of the SPIO distributions along the x-direction, the estimated relaxation times deviate with respect to those in more central regions. While this is an undesired effect of low MPI signal, color overlay image naturally eliminates these low-pixel-intensity regions to provide a clean multi-color MPI image, as seen in Fig. 4.6c.

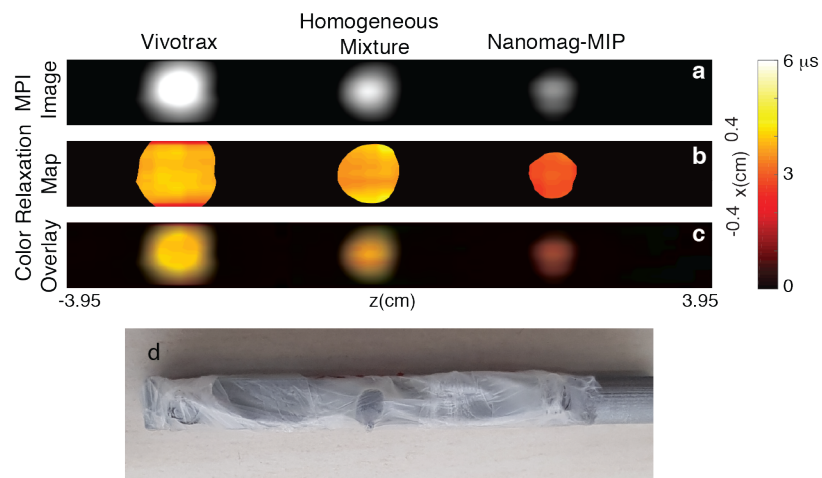


Figure 4.6: Calibration-free multi-color MPI results in 2D. The imaging experiment was conducted at 9.7 kHz and 15 mT-peak drive field, using Nanomag-MIP and VivoTrax SPIOs, and their homogeneous mixture. (a) The reconstructed x-space MPI image and (b) the corresponding multi-color relaxation map. (c) The color overlay of the MPI image and the multi-color map shows that the two nanoparticles and their homogeneous mixture can be clearly distinguished in 2D, solely based on their relaxation responses. The mixture yields a τ value that closely matches the signal-weighted average of the τ values from Nanomag-MIP and VivoTrax. (d) A photo of the imaged phantom with three tubes containing VivoTrax, the homogeneous mixture, and Nanomag-MIP from left to right, separated at 15 mm distances.

Chapter 5

Discussion

Multi-color MPI is a very promising extension of MPI due to its potential use in cardiovascular interventions, temperature mapping, and viscosity mapping. There has been significant progress in multi-color MPI, both via SFR and x-space reconstruction techniques. While these methods were shown to work exceptionally well, they either require extensive calibration for every SPIO types used [27] or multiple scans of the imaging FOV at different drive field amplitudes [40]. In this thesis, a calibration-free approach for multi-color MPI have been proposed and experimentally demonstrated, that works successfully with a single scan at a single drive field amplitude. Here, *calibration-free* refers to SPIO identification through their relaxation times, which are estimated *directly* from the MPI signal without any prior information. Note that while relaxation times can be measured in a calibration-free fashion, for certain applications such as viscosity or temperature mapping, one must obtain prior fiducial measurements to create a dictionary of relaxation times corresponding to specific environmental conditions. These measurements could be performed on an MPS setup within seconds, or on an MPI scanner within minutes. Alternatively, these measurements could be obtained directly during imaging via placing the fiducials next to the object of interest and imaging with a slightly extended FOV.

5.1 Effects of SPIO Types and Imaging Parameters

Distinguishable SPIO behavior is a fundamental requirement for any multi-color MPI technique. SFR-based methods have the advantage of being able to distinguish nanoparticles with different responses, independent of whether that difference stems from the harmonic or the relaxation responses. Still, Rahmer *et al.* have stated that, SPIOs with similar size distributions or similar hysteresis behavior would be difficult to separate [27]. In case of the proposed method, SPIOs are required to have distinct relaxation time constants for a clear differentiation. For the experimental results shown in this work, all three nanoparticles involved were multi-core SPIOs, with Perimag and Nanomag-MIP having similar chemical compositions and hydrodynamic diameters. Despite these similarities, the proposed multi-color MPI technique successfully distinguished these nanoparticles. To further improve the performance of this technique, two different approaches can be undertaken: SPIOs that are specifically tailored to have different relaxation behaviors would facilitate relaxation mapping. In addition, imaging parameters can be optimized to maximize the contrast between relaxation times. A previous work has compared the relaxation times of multi-core Resovist nanoparticles with single-domain UW33 nanoparticles, which had significantly different relaxation times. Interestingly, the ratio of the relaxation times remained almost constant (around 2-2.5) across a wide range of frequencies and drive field amplitudes [43]. These results suggest that, for such cases, the proposed method can be successfully applied at a variety of drive field parameters.

5.2 Resolution of the Relaxation Map

The pixel size in the relaxation map is equal to the distance between adjacent pFOV centers, which is a function of both the drive field amplitude and the overlap percentage. For the 2D imaging example in this work, this resolution

is equal to approximately 1.9 mm along the z-direction and 1 mm along the x-direction. Note, however, that the resolution of our MPI scanner is approximately 4 mm along the z-direction (for Nanomag-MIP nanoparticles). Hence, the true resolution of the relaxation map is still equal to the resolution of the MPI system, as that is the dominant factor under the given imaging conditions (see Supp. Fig. S1 for a detailed resolution analysis).

For MPI systems that have higher gradient selection fields or when using MPI-optimized nanoparticles, the resolution of the relaxation map may be worse than that of the MPI system. One method to mitigate this problem would be to use high overlap percentages. While this solution may sound unpractical, it is actually necessitated by the human safety limits [13, 14, 15, 16, 17, 50]. Operating at the safety limits, a linearly-ramping focus field with 20 T/s slew rate together with a 7 mT-peak drive field at 25 kHz results in 97% overlap between adjacent pFOVs. With that said, it is not uncommon for functional imaging techniques to possess lower resolution than their anatomical counterparts. For example, functional MRI or diffusion-weighted MRI both have significantly lower resolutions when compared to anatomical MRI.

5.3 Fine Tuning of the Hardware Delays

In this work, the t_{edge} parameter achieves a fine tuning of the system delay (e.g., correction of sub-sample delays), as needed for accurate relaxation time estimation. A prior calibration of the global hardware delay can further increase the speed of the search algorithm via restricting the possible ranges for t_{edge} . Note that this procedure is similar to the delay calibration procedure in MRI scanners. The delay between the applied gradient fields and data acquisition is calibrated globally for every MRI scanner, individually. Still, certain imaging procedures such as echo planar imaging (EPI) can be particularly sensitive to even small amounts of inaccuracies in this delay. Hence, a fine tuning of delays is performed every time an EPI image is acquired, using a reference scan data [51]. For the method proposed in this work, neither a global calibration nor a reference scan

is necessitated, as the delay can be estimated simultaneously with the relaxation time constant.

5.4 Towards True Quantitative MPI

While quantitative imaging is a desirable feature in MPI, environmental factors such as viscosity and temperature, as well as usage of different nanoparticle types may complicate quantitative imaging of iron concentration. SFR-based multi-color MPI approaches restore quantitiveness via individually calibrating the responses for different nanoparticles/conditions [27]. The technique proposed in this work can also be extended to restore quantitiveness for x-space MPI images. For a fixed nanoparticle type, the effects of environmental factors can be reversed by deconvolving the signals with the estimated relaxation kernels to yield a quantitative MPI image. In the case of different nanoparticles, the multi-color relaxation map can be used to generate separate x-space MPI images of each nanoparticle type, which can then be deconvolved by their respective measured PSFs and recombined to form a quantitative MPI image. For this latter approach, the PSFs could be measured either via a prior MPS measurement performed within seconds or by incorporating point source fiducials into the imaging volume, with a slight increase in scan time. Alternatively, a phantom made of point source fiducials could be imaged separately within a few minutes. Note that for SFR-based multi-color MPI approaches, such calibration scans last for hours for each nanoparticle type or environmental condition.

5.5 Extensions to 2D/3D Excitation and FFL Scanners

The Lissajous trajectory is a widely popular and efficient way of scanning the imaging volume due to its short imaging durations and comprehensive coverage

[52, 53]. For the proposed method to work for 2D/3D excitations such as the Lissajous trajectory, the FFP trajectory can be modified to produce data in opposing scan directions. Assuming that the non-adiabatic MPI signal model in [42] still applies, this modification could be achieved by scanning the same volume twice, with the excitation fields reversed in the second round. The signal could then be analyzed in local chunks to generate multi-color images.

The proposed method is not necessarily designed for FFP scanners and could potentially be extended to FFL scanners, after necessary modifications. Previous work has demonstrated that the non-adiabatic MPI signal model also applies in the case of 1D excitation in an FFL system [54]. Hence, the underlying time constant estimation method is expected to work as it is. However, akin to the inhomogeneous mixture case, signal contributions from different regions along the FFL may result in incorrect relaxation time constant estimations. Hence, similar to Phase 4 of the proposed algorithm, a recovery scheme must be developed to handle those special cases. A subsequent reconstruction algorithm based on filtered back projection can be used to reconstruct 3D multi-color images. Extending the proposed method to trajectories with multidimensional drive fields or FFL scanners remain as important future works.

Chapter 6

Conclusion

In this thesis, a novel calibration-free multi-color MPI technique was proposed, with results demonstrated via both MPS and imaging experiments. The proposed technique relies on distinguishing nanoparticles based on their relaxation response, where the relaxation time is directly estimated from the MPI signal via restoring the underlying mirror symmetry. A step-by-step algorithm is proposed to generate an accurate relaxation map (or multi-color MPI image) from the time constant estimations for each pFOV. The imaging results show that different nanoparticle responses can be successfully distinguished, without any calibration or prior information regarding their responses. The proposed calibration-free multi-color MPI technique is a promising method for future functional imaging applications of MPI, such as catheter tracking, viscosity mapping, temperature mapping, and stem cell tracking. Future work includes the utilization of this technique in quantitative imaging applications, and extensions to multidimensional trajectories and other MPI scanner topologies.

Bibliography

- [1] B. Gleich and J. Weizenecker, “Tomographic imaging using the nonlinear response of magnetic particles,” *Nature*, vol. 435, no. 7046, pp. 1214–1217, 2005.
- [2] J. Weizenecker, J. Borgert, and B. Gleich, “A simulation study on the resolution and sensitivity of magnetic particle imaging,” *Phys Med Biol*, vol. 52, no. 21, pp. 6363–6374, 2007.
- [3] P. W. Goodwill, E. U. Saritas, L. R. Croft, T. N. Kim, K. M. Krishnan, D. V. Schaffer, and S. M. Conolly, “X-Space MPI: Magnetic Nanoparticles for Safe Medical Imaging,” *Adv Mater*, vol. 24, no. 28, pp. 3870–3877, 2012.
- [4] E. U. Saritas, P. W. Goodwill, L. R. Croft, J. J. Konkle, K. Lu, B. Zheng, and S. M. Conolly, “Magnetic Particle Imaging (MPI) for NMR and MRI researchers,” *J Magn Reson*, vol. 229, no. C, pp. 116–126, 2013.
- [5] L. M. Bauer, S. F. Situ, M. A. Griswold, and A. C. S. Samia, “Magnetic Particle Imaging Tracers: State-of-the-Art and Future Directions,” *J Phys Chem Lett*, vol. 6, no. 13, pp. 2509–2517, 2015.
- [6] J. Weizenecker, B. Gleich, J. Rahmer, H. Dahnke, and J. Borgert, “Three-dimensional real-time in vivo magnetic particle imaging,” *Phys Med Biol*, vol. 54, no. 5, pp. L1–L10, 2009.
- [7] K. Lu, P. W. Goodwill, E. U. Saritas, B. Zheng, and S. M. Conolly, “Linearity and shift invariance for quantitative magnetic particle imaging,” *IEEE Trans Med Imaging*, vol. 32, no. 9, pp. 1565–1575, 2013.

- [8] B. Zheng, T. Vazin, P. W. Goodwill, A. Conway, A. Verma, E. U. Saritas, D. Schaffer, and S. M. Conolly, “Magnetic Particle Imaging tracks the long-term fate of in vivo neural cell implants with high image contrast,” *Sci Rep*, vol. 5, p. 14055, 2015.
- [9] B. Zheng, M. P. von See, E. Yu, B. Gunel, K. Lu, T. Vazin, D. V. Schaffer, P. W. Goodwill, and S. M. Conolly, “Quantitative Magnetic Particle Imaging Monitors the Transplantation, Biodistribution, and Clearance of Stem Cells In Vivo,” *Theranostics*, vol. 6, no. 3, pp. 291–301, 2016.
- [10] K. Them, J. Salamon, P. Szwargulski, S. Sequeira, M. G. Kaul, C. Lange, H. Ittrich, and T. Knopp, “Increasing the sensitivity for stem cell monitoring in system-function based magnetic particle imaging,” *Phys Med Biol*, vol. 61, no. 9, pp. 3279–3290, 2016.
- [11] J. Haegele, J. Rahmer, B. Gleich, J. Borgert, H. Wojtczyk, N. Panagiotopoulos, T. M. Buzug, J. Barkhausen, and F. M. Vogt, “Magnetic particle imaging: visualization of instruments for cardiovascular intervention.,” *Radiology*, vol. 265, pp. 933–938, dec 2012.
- [12] E. Yu, M. Bishop, P. W. Goodwill, B. Zheng, M. Ferguson, K. M. Krishnan, and S. M. Conolly, “First Murine in vivo Cancer Imaging with MPI,” in *Proc. 6rd Int. Workshop Magn. Particle Imag.*, (Lbeck, Germany), p. 148, 2016.
- [13] I. Schmale, B. Gleich, J. Schmidt, J. Rahmer, C. Bontus, R. Eckart, B. David, M. Heinrich, O. Mende, O. Woywode, J. Jokram, and J. Borgert, “Human PNS and SAR study in the frequency range from 24 to 162 kHz,” in *Proc. 3rd Int. Workshop Magn. Particle Imag.*, (Berkeley, USA), p. 1, 2013.
- [14] E. U. Saritas, P. W. Goodwill, G. Z. Zhang, and S. M. Conolly, “Magnetostimulation Limits in Magnetic Particle Imaging,” *IEEE Trans Med Imaging*, vol. 32, no. 9, pp. 1600–1610, 2013.

- [15] I. Schmale, B. Gleich, J. Rahmer, C. Bontus, J. Schmidt, and J. Borgert, “MPI Safety in the View of MRI Safety Standards,” *IEEE Trans Magn*, vol. 51, no. 2, pp. 1–4, 2015.
- [16] E. U. Saritas, P. W. Goodwill, and S. M. Conolly, “Effects of pulse duration on magnetostimulation thresholds,” *Med Phys*, vol. 42, no. 6, pp. 3005–3012, 2015.
- [17] O. Demirel and E. Saritas, “Effects of duty cycle on magnetostimulation thresholds in mpi,” *Intern J Magnetic Particle Imaging*, vol. 3, no. 1, 2017.
- [18] P. W. Goodwill, J. J. Konkle, B. Zheng, E. U. Saritas, and S. M. Conolly, “Projection x-space magnetic particle imaging,” *IEEE Trans Med Imaging*, vol. 31, no. 5, pp. 1076–1085, 2012.
- [19] P. Goodwill, L. Croft, J. Konkle, K. Lu, E. Saritas, B. Zheng, and S. Conolly, *Third Generation X-Space MPI Mouse and Rat Scanner*, pp. 261–265. Berlin, Heidelberg: Springer Berlin Heidelberg, 2012.
- [20] P. W. Goodwill, L. R. Croft, J. J. Konkle, K. Lu, E. U. Saritas, B. Zheng, and S. M. Conolly, “A 7 T/M 3D x-space MPI mouse and rat scanner,” in *Proc. 3rd Int. Workshop Magn. Particle Imag.*, (Berkeley, USA), p. 1, 2013.
- [21] J. Rahmer, J. Weizenecker, B. Gleich, and J. Borgert, “Signal encoding in magnetic particle imaging: properties of the system function,” *BMC Med Imaging*, vol. 9, no. 1, pp. 4–21, 2009.
- [22] T. Knopp, T. F. Sattel, S. Biederer, J. Rahmer, J. Weizenecker, B. Gleich, J. Borgert, and T. M. Buzug, “Model-based reconstruction for magnetic particle imaging,” *IEEE Trans Med Imaging*, vol. 29, no. 1, pp. 12–18, 2010.
- [23] T. Knopp, J. Rahmer, T. F. Sattel, S. Biederer, J. Weizenecker, B. Gleich, J. Borgert, and T. M. Buzug, “Weighted iterative reconstruction for magnetic particle imaging,” *Phys Med Biol*, vol. 55, no. 6, pp. 1577–1589, 2010.

- [24] J. Rahmer, J. Weizenecker, B. Gleich, and J. Borgert, “Analysis of a 3-D System Function Measured for Magnetic Particle Imaging,” *IEEE Trans Med Imaging*, vol. 31, no. 6, pp. 1289–1299, 2012.
- [25] P. W. Goodwill and S. M. Conolly, “The X-Space Formulation of the Magnetic Particle Imaging Process: 1-D Signal, Resolution, Bandwidth, SNR, SAR, and Magnetostimulation,” *IEEE Trans Med Imaging*, vol. 29, no. 11, pp. 1851–1859, 2010.
- [26] P. W. Goodwill and S. M. Conolly, “Multidimensional X-Space Magnetic Particle Imaging,” *IEEE Trans Med Imaging*, vol. 30, no. 9, pp. 1581–1590, 2011.
- [27] J. Rahmer, A. Halkola, B. Gleich, I. Schmale, and J. Borgert, “First experimental evidence of the feasibility of multi-color magnetic particle imaging,” *Phys Med Biol*, pp. 1775–1791, 2015.
- [28] J. Haegele, N. Panagiotopoulos, S. Cremers, J. Rahmer, J. Franke, R. L. Duschka, S. Vaalma, M. Heidenreich, J. Borgert, P. Borm, J. Barkhausen, and F. M. Vogt, “Magnetic Particle Imaging: A Resovist Based Marking Technology for Guide Wires and Catheters for Vascular Interventions,” *IEEE Trans Med Imaging*, vol. 35, no. 10, pp. 2312–2318, 2016.
- [29] N. Nothnagel, J. Rahmer, B. Gleich, A. Halkola, T. M. Buzug, and J. Borgert, “Steering of Magnetic Devices With a Magnetic Particle Imaging System,” *IEEE Trans Bio-Med Eng*, vol. 63, no. 11, pp. 2286–2293, 2016.
- [30] J. Rahmer, D. Wirtz, C. Bontus, J. Borgert, and B. Gleich, “Interactive Magnetic Catheter Steering with 3D Real-Time Feedback Using Multi-Color Magnetic Particle Imaging,” *IEEE Trans Med Imaging*, pp. 1–1, 2017.
- [31] C. Stehning, B. Gleich, and J. Rahmer, “Simultaneous magnetic particle imaging (mpi) and temperature mapping using multi-color mpi,” *Intern J Magnetic Particle Imaging*, vol. 2, no. 2, 2016.
- [32] A. M. Rauwerdink and J. B. Weaver, “Measurement of molecular binding using the Brownian motion of magnetic nanoparticle probes,” *Appl Phys Lett*, vol. 96, no. 3, pp. 033702–4, 2010.

- [33] S. Bhaskar, F. Tian, T. Stoeger, W. Kreyling, J. M. de la Fuente, V. Grazu, P. Borm, G. Estrada, V. Ntziachristos, and D. Razansky, “Multifunctional nanocarriers for diagnostics, drug delivery and targeted treatment across blood-brain barrier: perspectives on tracking and neuroimaging,” *Part Fibre Toxicol*, vol. 7, no. 1, p. 3, 2010.
- [34] A. M. Rauwerdink and J. B. Weaver, “Viscous effects on nanoparticle magnetization harmonics,” *J Magn Magn Mater*, vol. 322, no. 6, pp. 609–613, 2009.
- [35] J. B. Weaver, A. M. Rauwerdink, and E. W. Hansen, “Magnetic nanoparticle temperature estimation,” *Med Phys*, vol. 36, no. 5, pp. 1822–1829, 2009.
- [36] T. Wawrzik, C. Kuhlmann, H. Remmer, N. Gehrke, A. Briel, M. Schilling, and F. Ludwig, “Effect of brownian relaxation in frequency-dependent magnetic particle spectroscopy measurements,” in *Proc. 3rd Int. Workshop Magn. Particle Imag.*, (Berkeley, USA), p. 1, 2013.
- [37] M. Hofmann, J. Dieckhoff, H. Ittrich, and T. Knopp, “Experimental distinction of different viscosities using multispectral magnetic particle imaging,” in *Proc. 6th Int. Workshop Magn. Particle Imag.*, (Lbeck, Germany), p. 9, 2016.
- [38] M. Utkur, Y. Muslu, and E. U. Saritas, “Relaxation-based viscosity mapping for magnetic particle imaging,” *Phys Med Biol*, vol. 62, no. 9, p. 3422, 2017.
- [39] T. Viereck, C. Kuhlmann, S. Draack, M. Schilling, and F. Ludwig, “Dual-frequency magnetic particle imaging of the brownian particle contribution,” *J Magn Magn Mater*, vol. 427, no. Supplement C, pp. 156 – 161, 2017.
- [40] D. Hensley, P. Goodwill, L. Croft, and S. Conolly, “Preliminary experimental x-space color MPI,” in *Proc. 5th Int. Workshop Magn. Particle Imag.*, (Istanbul, Turkey), p. 1, 2015.
- [41] S. A. Shah, D. B. Reeves, R. M. Ferguson, J. B. Weaver, and K. M. Krishnan, “Mixed brownian alignment and néel rotations in superparamagnetic iron oxide nanoparticle suspensions driven by an ac field,” *Phys. Rev. B*, vol. 92, p. 094438, Sep 2015.

- [42] L. R. Croft, P. W. Goodwill, and S. M. Conolly, “Relaxation in X-Space Magnetic Particle Imaging,” *IEEE Trans Med Imaging*, vol. 31, no. 12, pp. 2335–2342, 2012.
- [43] L. R. Croft, P. W. Goodwill, J. J. Konkle, H. Arami, D. A. Price, A. X. Li, E. U. Saritas, and S. M. Conolly, “Low drive field amplitude for improved image resolution in magnetic particle imaging,” *Med Phys*, vol. 43, no. 1, pp. 424–435, 2015.
- [44] Y. Muslu, M. Utkur, O. B. Demirel, and E. U. Saritas, “Calibration-free color MPI,” in *Proc. 6th Int. Workshop Magn. Particle Imag.*, (Lbeck, Germany), p. 10, 2016.
- [45] G. Onuker and E. U. Saritas, “Simultaneous relaxation estimation and image reconstruction in MPI,” in *Proc. 5th Int. Workshop Magn. Particle Imag.*, (Istanbul, Turkey), p. 1, 2015.
- [46] K. Lu, P. W. Goodwill, E. U. Saritas, B. Zheng, and S. M. Conolly, “Linearity and Shift Invariance for Quantitative Magnetic Particle Imaging,” *IEEE Trans Med Imaging*, vol. 32, no. 9, pp. 1565–1575, 2013.
- [47] J. J. Konkle, P. W. Goodwill, D. W. Hensley, R. D. Orendorff, M. Lustig, and S. M. Conolly, “A Convex Formulation for Magnetic Particle Imaging X-Space Reconstruction,” *PLOS ONE*, vol. 10, no. 10, pp. e0140137–15, 2015.
- [48] J. MacQueen, “Some methods for classification and analysis of multivariate observations,” in *Proc. of the Fifth Berkeley Symposium on Mathematical Statistics and Probability, Volume 1: Statistics*, (Berkeley, Calif.), pp. 281–297, University of California Press, 1967.
- [49] R. M. Ferguson, A. P. Khandhar, S. J. Kemp, H. Arami, E. U. Saritas, L. R. Croft, J. Konkle, P. W. Goodwill, A. Halkola, J. Rahmer, J. Borgert, S. M. Conolly, and K. M. Krishnan, “Magnetic Particle Imaging With Tailored Iron Oxide Nanoparticle Tracers,” *IEEE Trans Med Imaging*, vol. 34, no. 5, pp. 1077–1084, 2015.

- [50] J. J. Konkle, P. W. Goodwill, E. U. Saritas, B. Zheng, K. Lu, and S. M. Conolly, “Twenty-fold acceleration of 3D projection reconstruction MPI,” *Biomedizinische Technik/Biomedical Engineering*, vol. 58, no. 6, pp. 565–576, 2013.
- [51] H. Bruder, H. Fischer, H.-E. Reinfelder, and F. Schmitt, “Image reconstruction for echo planar imaging with nonequidistant k-space sampling,” *Magn Reson Med*, vol. 23, no. 2, pp. 311–323, 1992.
- [52] C. Kaethner, W. Erb, M. Ahlborg, P. Szwargulski, T. Knopp, and T. M. Buzug, “Non-equispaced system matrix acquisition for magnetic particle imaging based on lissajous node points,” *IEEE Trans Med Imaging*, vol. 35, no. 11, pp. 2476–2485, 2016.
- [53] T. Knopp, S. M. Conolly, and T. M. Buzug, “Recent progress in magnetic particle imaging: from hardware to preclinical applications,” *Phys Med Biol*, vol. 62, no. 9, p. E4, 2017.
- [54] K. Bente, M. Weber, M. Graeser, T. F. Sattel, M. Erbe, and T. M. Buzug, “Electronic field free line rotation and relaxation deconvolution in magnetic particle imaging,” *IEEE Trans Med Imaging*, vol. 34, no. 2, pp. 644–651, 2015.

Appendix A

Relaxation Time Constant of a Homogeneous Mixture

As first stated in Section 3.4, when two different SPIOs are mixed homogeneously, $\hat{\tau}$ is the weighted average of the relaxation time constants of the two SPIOs. Here, the mixture is assumed to be completely homogeneous and the two SPIOs have identical adiabatic signals, $s_{\text{half}}(t)$ (e.g., bound/unbound SPIOs with identical nanoparticle core sizes). Therefore, Eqs. 3.2 and 3.3 can be modified as follows:

$$s_{\text{pos}}(t) = c_1 s_{\text{half}}(t) * r_1(t) + c_2 s_{\text{half}}(t) * r_2(t) \quad (\text{A.1})$$

$$s_{\text{neg}}(t) = c_1 (-s_{\text{half}}(-t) * r_1(t)) + c_2 (-s_{\text{half}}(-t) * r_2(t)) \quad (\text{A.2})$$

Here, c_1 and c_2 are the concentrations of the two different SPIOs, and $r_1(t)$ and $r_2(t)$ are the corresponding relaxation kernels with $\tau_1 \neq \tau_2$. Fourier domain representation of Eqs. A.1 and A.2 can be written as follows:

$$R_j(f) = \frac{1}{1 + i2\pi f\tau_j}, \quad j = 1, 2 \quad (\text{A.3})$$

$$S_{\text{pos}}(f) = S_{\text{half}}(f) \cdot (c_1 R_1(f) + c_2 R_2(f)) \quad (\text{A.4})$$

$$S_{\text{neg}}(f) = -S_{\text{half}}^*(f) \cdot (c_1 R_1(f) + c_2 R_2(f)) \quad (\text{A.5})$$

Here, there are three unknowns, S_{half} , $R_1(f)$, and $R_2(f)$, and two equations,

Eq. A.4 and A.5. Hence, the equation set above is underdetermined. Nevertheless, if the original estimation method given in Eq. 3.7 is applied, the following expression can be obtained using Eqs. A.4-A.5.:

$$\begin{aligned}\tau(f) &= \frac{S_{\text{pos}}^*(f) + S_{\text{neg}}(f)}{i2\pi f(S_{\text{pos}}^*(f) - S_{\text{neg}}(f))} \\ &= \frac{2c_1\tau_1(1 + 4\pi^2 f^2 \tau_2^2) + 2c_2\tau_2(1 + 4\pi^2 f^2 \tau_1^2)}{2c_1(1 + 4\pi^2 f^2 \tau_2^2) + 2c_2(1 + 4\pi^2 f^2 \tau_1^2)}\end{aligned}\quad (\text{A.6})$$

Equation A.6 is not strictly linear with respect to concentrations of the SPIOs in the mixture. However, for small frequencies (e.g., for $f < 4f_0$ where f_0 is the drive field frequency), the terms $(1 + 4\pi^2 f^2 \tau_i^2)$ can be approximated as 1. In that case, Eq. A.6 simplifies to the following form:

$$\tau(f) \approx \frac{c_1\tau_1 + c_2\tau_2}{c_1 + c_2}\quad (\text{A.7})$$

where $\tau(f)$ is equal to the weighted average of τ_1 and τ_2 . Simulation results presented in Fig. 4.3d confirm that Eq. A.7 behaves linearly with respect to relaxation time constants and the relative concentrations in the mixture.

Note that, if the adiabatic responses of the two SPIOs are different (e.g., SPIOs with different core sizes), the estimated $\tau(f)$ will be an average of τ_1 and τ_2 , weighted by the overall signal levels from the two SPIOs. In addition, an SPIO sample may exhibit a spread of τ values, e.g., due to polydispersity in nanoparticle size. For that case, the estimated relaxation time constant will be an average over the spread of τ values, weighted by their relative signal contributions.

Appendix B

Effects of pFOV overlap on the Relaxation Map

A 1D simulation study was performed to investigate the effects of pFOV overlap percentage on the resolution of the relaxation map. The results are given in Fig. B.1. The simulation parameters were: 3 T/m/ μ_0 selection field gradient, 10 mT-peak drive field at 10 kHz, and 21 nm nanoparticle diameter. The resulting pFOV size was 6.7 mm, with 2.5 mm MPI system resolution for x-space reconstructed images. The simulations were performed for 90%, 80%, 60%, and 40% overlaps. For all four cases, the resolutions of the MPI images remain the same due to x-space reconstruction. In the relaxation map, one τ value is assigned to the center of each pFOV. Therefore, the pixel size of the relaxation map is equal to the distance between the neighboring pFOVs, corresponding to 0.67 mm, 1.3 mm, 2.67 mm, and 4 mm for the tested overlaps, respectively. For 90% and 80% overlaps, despite the smaller pixel sizes, the resolutions of the relaxation maps are dominated by the intrinsic resolution of the MPI system. For smaller overlap cases, however, the pixel size gets larger than the resolution of the MPI system. In return, the resolution of the relaxation map is dominated by its own pixel size, causing a deterioration in the quality of the maps. Therefore, to preserve the resolution of the relaxation map, the overlap percentage should ideally be chosen to yield a pixel size smaller than the resolution of the MPI system.

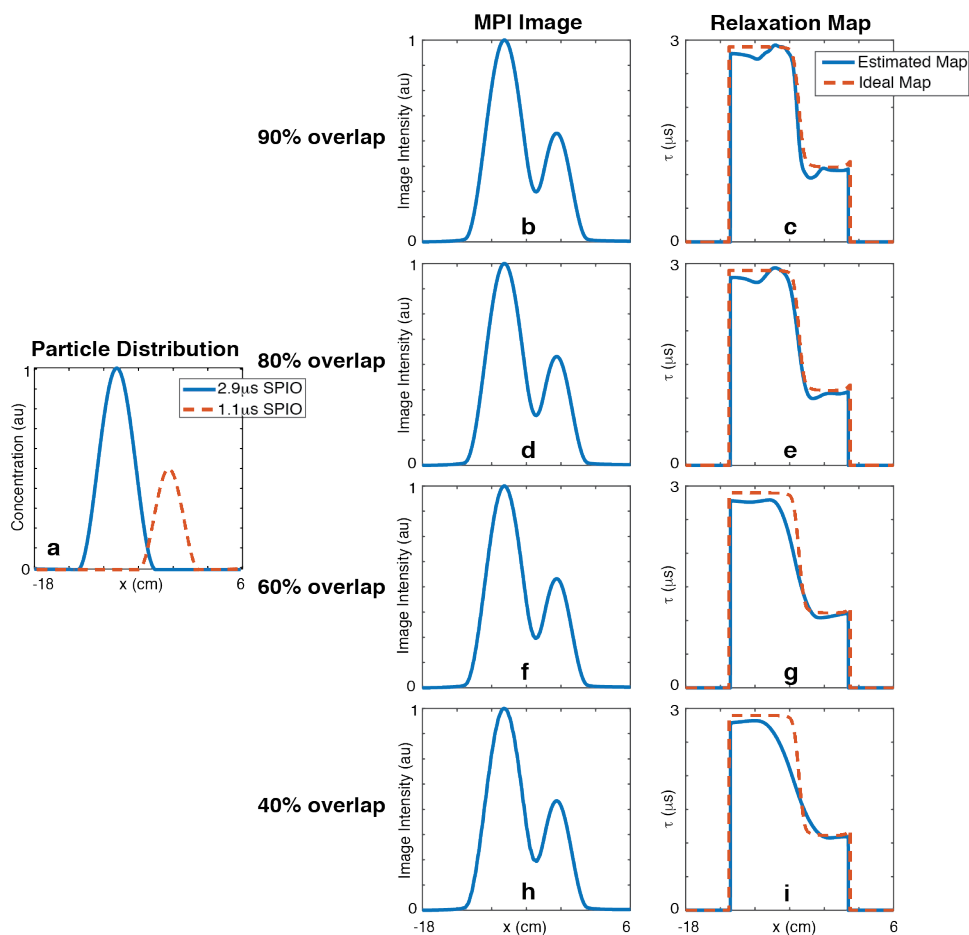


Figure B.1: Results of the resolution study. (a) Nanoparticle distributions with two distinct τ values. Each row demonstrates a simulation result for a different pFOV overlap (e.g. 90%, 80%, 60% and 40%). For the first two rows, the resolution of the MPI system is larger than the spatial overlap (or pixel size) of the pFOVs. As such, the resolution of the relaxation map is equal to the resolution of the MPI system. For the last two rows, the pixel size of the relaxation map is larger than the resolution of the MPI system. Accordingly, the resolution of the relaxation map is equal to the pixel size of the relaxation map.

Appendix C

Local Minima Analysis

C.1 The Effects of Hardware Delays

In Section 3.1, Eq. 3.7 presented a technique to estimate τ directly from the MPI signal. However, as given in Section 3.2, the experimental implementation of this technique requires a fine tuning of the hardware delays via the parameter t_{edge} . Below, the effect of an error in t_{edge} on the resulting τ estimation is mathematically derived.

Here, an error in t_{edge} can be modeled as a leftover time delay, t_d , in the MPI signal given in Eq. 2.9. For that case, the positive and negative half cycles of the delayed MPI signal can be expressed as:

$$s_{\text{pos,del}}(t) = s_{\text{pos}}(t) \tag{C.1}$$

$$s_{\text{neg,del}}(t) = s_{\text{neg}}(t) \tag{C.2}$$

Equations C.1 and C.2 can be transformed into Fourier domain as follows:

$$S_{\text{pos,del}}(f) = S_{\text{pos}}(f) \cdot e^{-i2\pi f t_d} = S_{\text{half}}(f) \cdot R(f) \cdot e^{-i2\pi f t_d} \tag{C.3}$$

$$S_{\text{neg,del}}(f) = S_{\text{neg}}(f) \cdot e^{-i2\pi f t_d} = -S_{\text{half}}^*(f) \cdot R(f) \cdot e^{-i2\pi f t_d} \tag{C.4}$$

Here, $S_{\text{pos,del}}(f)$ and $S_{\text{neg,del}}(f)$ denote the Fourier transforms of time delayed positive and negative half cycles. The second equalities in these expressions follow directly from Eqs. 3.5 and 3.6, where $S_{\text{half}}(f)$ is the Fourier transform of half a period of the adiabatic MPI signal and $R(f)$ is the Fourier transform of the relaxation kernel.

If the equations above are directly substituted into Eq.3.7 for estimating the relaxation time constant:

$$\tilde{\tau}(f) = \frac{S_{\text{pos,del}}^*(f) + S_{\text{neg,del}}(f)}{i2\pi f(S_{\text{pos,del}}^*(f) - S_{\text{neg,del}}(f))} \quad (\text{C.5})$$

$$= \frac{(1 + i2\pi f\tau) \cdot e^{i2\pi ft_d} - (1 - i2\pi f\tau) \cdot e^{-i2\pi ft_d}}{i2\pi f((1 + i2\pi f\tau) \cdot e^{i2\pi ft_d} + (1 - i2\pi f\tau) \cdot e^{-i2\pi ft_d})} \quad (\text{C.6})$$

$$= \frac{1}{2\pi f} \frac{\text{Im} \{(1 + i2\pi f\tau) \cdot e^{i2\pi ft_d}\}}{\text{Re} \{(1 + i2\pi f\tau) \cdot e^{i2\pi ft_d}\}} \quad (\text{C.7})$$

Here, $\tilde{\tau}(f)$ is the erroneous estimate due to leftover time delay and τ is the correct relaxation time constant. In these relations, $\tilde{\tau}(f)$ is incorrect due to the phase terms $e^{-i2\pi ft_d}$ and $e^{i2\pi ft_d}$. To show that $\tilde{\tau}(f)$ is equal to τ only for $t_d = 0$, Eq. B.7 can be manipulated as follows:

$$\tilde{\tau}(f) = \frac{1}{2\pi f} \tan(\angle((1 + i2\pi f\tau) \cdot e^{i2\pi ft_d})) \quad (\text{C.8})$$

$$= \frac{1}{2\pi f} \tan(\text{atan}(2\pi f\tau) + 2\pi ft_d) \quad (\text{C.9})$$

Here, $(\text{Im} \{z\})/(\text{Re} \{z\})$ is written as $\tan(\angle z)$, where \angle denote the angle of the complex number z , $\text{atan}(\cdot)$ denote the arctangent operation. Following that, $\tilde{\tau}(f)$ can be written as a multiplication of τ with a phase based error term:

$$\tilde{\tau}(f) = \frac{1}{2\pi f} \frac{2\pi f\tau + \tan(2\pi ft_d)}{1 - 2\pi f\tau \tan(2\pi ft_d)} \quad (\text{C.10})$$

$$= \tau \frac{1 + \frac{1}{2\pi f\tau} \tan(2\pi ft_d)}{1 - 2\pi f\tau \tan(2\pi ft_d)} \quad (\text{C.11})$$

Here, it can be seen that Eq. B.11 equals to τ for $\tan(2\pi ft_d) = 0$, equivalently $t_d = 0$. This expression can be further simplified by assuming a very small $2\pi ft_d$:

$$\tilde{\tau}(f) = \tau \frac{1 + \frac{t_d}{\tau}}{1 - 2\pi ft_d} \quad (\text{C.12})$$

Again, Eq. B.12 confirms the findings in Eq. B.11, i.e., the correct τ estimate is achieved for the case of $t_d = 0$. Equivalently, the correct τ estimate is achieved for the case of correct $t_{\text{edge}} = 0$.

C.2 Uniqueness of Local Minimum

Given in Fig. C.1 is a simulation study to show that Eq. 3.9 (i.e., the MSE between the positive and mirrored negative signals after the deconvolution) has a unique minimum at the correct $(\hat{\tau}, \hat{t}_{\text{edge}})$ pair. The simulation parameters were as follows: 3 T/m/ μ_0 gradient, 10 mT-peak drive field at 10kHz (corresponding to a drive field period of $T = 0.1$ ms), and 21 nm nanoparticle diameter. Simulations were run for a point source located at the center of the pFOV. Results for three different cases with different relaxation time constants are shown: 1 μs , 3 μs , and 5 μs . For each case, the correct t_{edge} value was zero. The results show the MSE in Eq. 3.9 in units of decibels (dB) for various $(\hat{\tau}, \hat{t}_{\text{edge}})$ pairs. For all cases, the MSE is minimized for the correct $(\hat{\tau}, \hat{t}_{\text{edge}})$ pair only (shown with red arrows). These results are consistent with Eqs. B.11 and B.12 presented above.

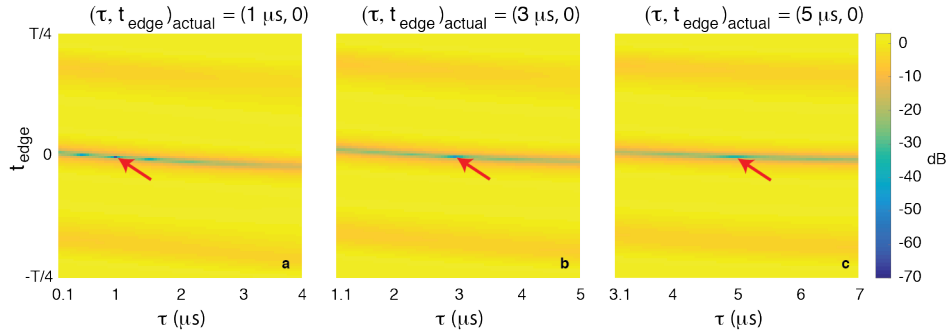


Figure C.1: Simulation results for the uniqueness of the local minimum of Eq. 3.9. Here, the logarithm of the MSE between the positive and mirrored negative signals after the deconvolution is calculated across different (τ, t_{edge}) pairs. The vertical axes show the range of t_{edge} , while the horizontal axes show the range of τ values. The simulation results for the actual pairs of (a) $(\tau, t_{\text{edge}})_{\text{actual}} = (1 \mu\text{s}, 0)$, (b) $(\tau, t_{\text{edge}})_{\text{actual}} = (3 \mu\text{s}, 0)$, and (c) $(\tau, t_{\text{edge}})_{\text{actual}} = (5 \mu\text{s}, 0)$. The correct pairs that minimize Eq. 3.9 are shown with red arrows.

Appendix D

Noise Analysis

A simulation study to test the robustness of the proposed relaxation time constant estimation technique against noise is presented below in Fig. D.1. Simulation parameters were as follows: 3 T/m/ μ_0 gradient, 10 mT-peak drive field at 10 kHz, 21 nm nanoparticle diameter, and assuming a point source located at the center of the pFOV. Simulations were run for three different relaxation time constants (1 μ s, 3 μ s, and 5 μ s), and 21 different SNR values ranging between 2-100. Here, SNR was defined as the maximum signal intensity (after the removal of fundamental frequency) divided by the standard deviation of the additive white Gaussian noise. The results display the mean values and standard deviations of the estimated τ values across different SNR levels. On average, the technique slightly underestimates the relaxation time for $\tau=1$ μ s (approximately 3% underestimation), slightly overestimates for $\tau=5$ μ s (approximately 2% overestimation), and provides very accurate results for $\tau=3$ μ s. Even at very low SNR values of SNR=2, the standard deviations in τ estimations are below 0.4 μ s for all three cases (i.e., less than 0.4% of the drive field period). For SNR values larger than 15, the standard deviations decrease to the order of 0.05 μ s for all three cases (i.e., less than 0.05% of the drive field period), demonstrating noise robustness of the proposed scheme.

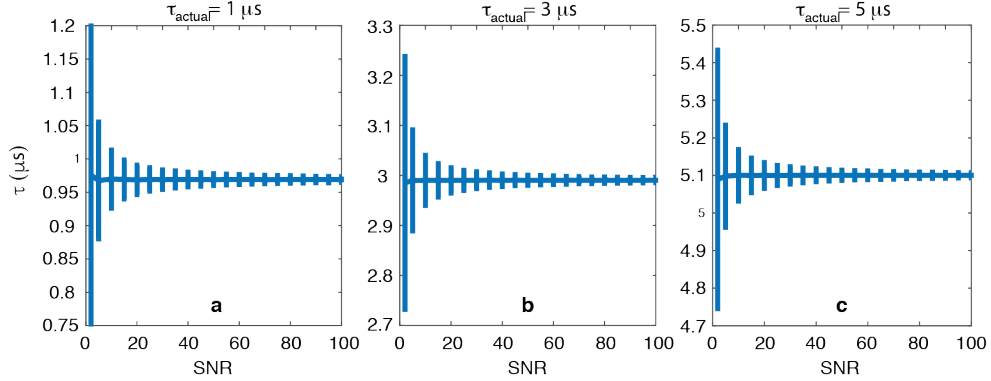


Figure D.1: Simulation results for the robustness of the proposed relaxation time constant estimation technique against noise. Here standard deviations of the estimated τ values are calculated across different SNR values. The vertical axes show the range of estimated τ , while the horizontal axes show the range of SNR values. Standard deviations for the actual time constant of (a) $\tau_{actual} = 1 \mu s$, (b) $\tau_{actual} = 3 \mu s$, and (c) $\tau_{actual} = 5 \mu s$.

A simulation study to test the robustness of the proposed calibration-free multi-color MPI algorithm against noise is presented below in Fig. D.2. Simulation parameters were as follows: 3 T/m/ μ_0 gradient, 10 mT-peak drive field at 10 kHz, and 21 nm nanoparticle diameter. Two different SPIOs with relaxation time constants of 2.9 μs and 1.1 μs were assumed. The relaxation mapping results remain fairly accurate even for very low SNR values of SNR=2. For larger SNR at or above SNR=5, relaxation maps demonstrate a strong robustness against noise, with a slight tendency to underestimate the relaxation time, as predicted in Fig. D.1. During these estimations, frequencies up to and including $4f_0$ were utilized (see Eq. 3.8). Since these frequencies contain a significant portion of the signal power, such a frequency restriction makes the relaxation mapping algorithm more robust against noise, as well.

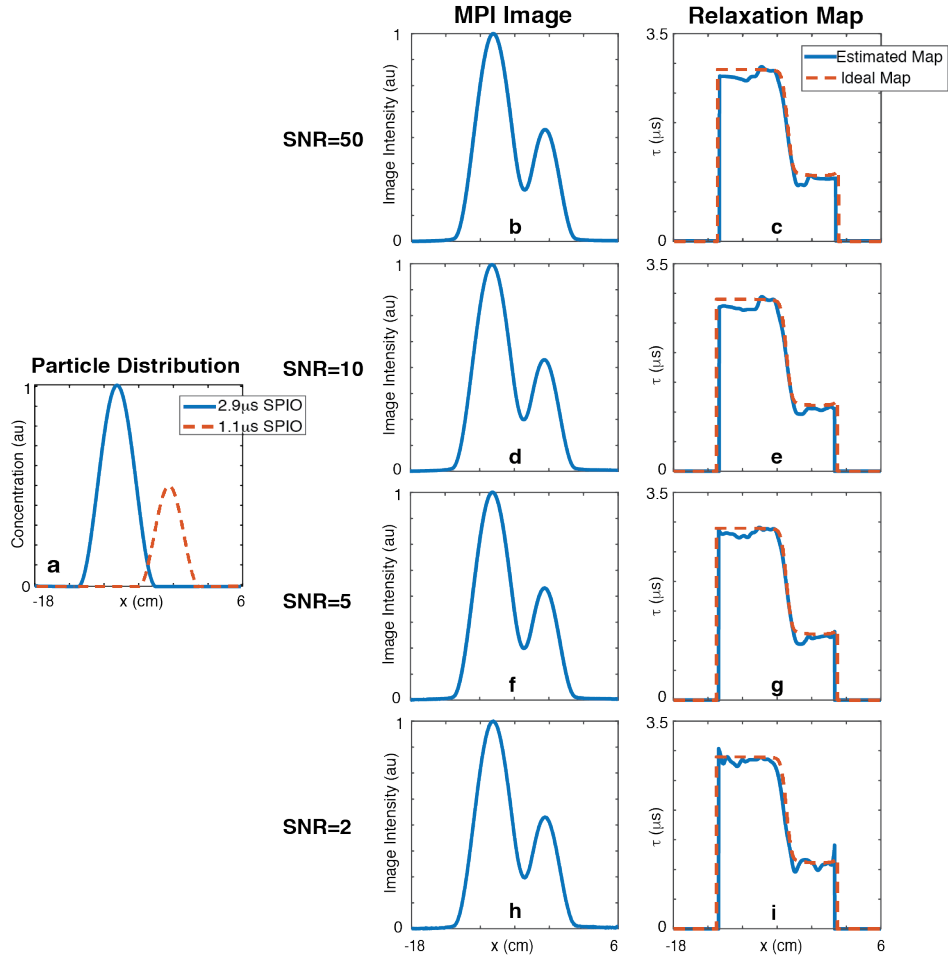


Figure D.2: Simulation results for the robustness of the proposed calibration-free multi-color MPI algorithm against noise. Each row demonstrates a simulation result for a different SNR value (e.g. 50, 10, 5, and 2). (a) Nanoparticle distributions with two distinct τ values. (c, e) For larger SNR values (e.g., SNR=10), results of the proposed mapping algorithm do not show significant deviations from each other. (g) For SNR=5 case, relaxation map shows very small, noise-like distortions, however shape of the map is still similar to that of SNR=50 case. (i) For SNR=2 case, there are larger deviations from the ideal map, but the results are still fairly accurate.